

**Carl von Ossietzky
Universität Oldenburg**

Course of studies:
Master of Science in Physics

MASTER'S THESIS

A laser-based spectral simulator

Submitted from: Tammo Sternke

Supervisors: Prof. Dr. Christoph Lienau
Dr. Annette Hammer

Oldenburg, November 17, 2010

To my parents

Abstract

We report on a method and apparatus for the generation of light with a given or user defined spectral distribution in the range from 480 nm to 1600 nm. A laser generated broadband supercontinuum is modulated in the frequency domain by a programmable liquid crystal display spatial light modulator (LCD-SLM) in an optical synthesizer. This design facilitates the high fidelity reproduction of a desired spectrum, e.g. AM0 and AM1.5G. With the average supercontinuum power of 4 W a solar cell of up to 6.75 mm² (at AM0) can be illuminated at a power of 1 kW/m² – thus one sun, which provides an interesting perspective for testing solar cells.

Terms and definitions

AM0	Air mass zero (spectrum), i.e. solar spectrum before it enters the atmosphere of the earth.
AM1.5G	Air mass 1.5 global (spectrum), i.e. solar spectrum after passing effectively through 1.5 atmospheres. The sun has to be at an angle of 48° with respect to the normal at the surface of the earth, while global denotes the inclusion of scattered light.
APE	Average photon energy
SLM	Spatial light modulator
LCD	Liquid crystal display
mask	Single LCD with 640 pixels used in the SLM.
bit-value	Integer number encoding the applied voltage $[0,10]$ V on one LCD-pixel at 12 bit resolution.
modulation	Gained phase in a single mask and pixel.
retardance	Synonym for modulation
WLS	Fiber-based supercontinuum white light source
darkbits	Set of 640 bit-values producing minimum transmission for all wavelengths when applied to the SLM.

Contents

1	Introduction	11
2	Some aspects of photovoltaic energy conversion	14
2.1	Multi-junction solar cells	14
2.2	The solar spectrum	19
3	Spatial light modulators	21
3.1	Functional principle of a spatial light modulator (SLM)	21
3.2	Amplitude modulation with a dual-mask SLM	24
4	Design of the experimental setup	28
4.1	Setup of an optical synthesizer	28
4.2	Selection of the components	29
4.2.1	Mirror selection	29
4.2.2	Raytracing	31
4.2.3	Raytracing for an off-axis mirror	34
4.2.4	Prism selection	35
4.3	Summary of the experimental setup	37
5	Calibration of the optical synthesizer	39
5.1	Wavelength to pixel-number mapping	39
5.2	Minimum transmission spectrum by applying 'darkbits'	41
6	Generation of arbitrary spectra	43
6.1	Calculation of bit-values for a desired spectrum	43
6.2	Feedback loop	45
6.3	Experimental simulation of various spectra	47
6.3.1	Experimental procedures	47
6.3.2	Flat spectrum	48
6.3.3	Reference spectra AM0 and AM1.5G	50
6.3.4	Summer and winter spectrum measured outdoors	51
6.4	A first test with a triple-junction solar cell	53

7	Conclusions and Outlook	56
	References	59
A	Appendix to Eq. 17	65
B	List of components	66
C	Reflection efficiencies for used coatings	68
D	Source code for MATLAB	69
	D.1 Raytracing	69
	D.2 SLM-control	74
	D.3 Prism deflection angle	78
E	Acknowledgements	79

List of Figures

1	Illustration of thermalization losses in a semiconductor after light absorption.	14
2	Structure of a InGaP/InGaAs/Ge triple-junction solar cell.	16
3	Current-voltage characteristic of a single pn-junction.	17
4	Examples for temporal variations of the solar spectrum.	20
5	Structure of one pixel in a twisted nematic LCD-SLM.	21
6	Reference modulation curve for a single-mask SLM at $\lambda = 633$ nm.	23
7	Mask alignment in a dual-mask SLM.	25
8	Schematic of a symmetric 4-f optical synthesizer.	28
9	Spectrum of the white light source before passing through the optical synthesizer.	30
10	Angle overview for the reflection of a light ray on a parabolic mirror.	33
11	Ray-tracing image for an on-axis mirror in the optical synthesizer.	34
12	Ray-tracing image for an off-axis mirror in the optical synthesizer.	35
13	Calculated difference in deflection angle between light with $\lambda = 480$ nm and $\lambda = 2325$ nm dispersed by an equilateral 60° prism for different material types.	36
14	Spectrum of the white light source after passing through the optical synthesizer.	38
15	Relation between pixel-numbers and wavelengths being addressed by them.	40
16	Bit-values producing minimum transmission (darkbits) as a function of the wavelength.	41
17	Difference modulation curve (DMC) for $\lambda = 633$ nm.	44
18	Electronic circuit for measuring the IV-characteristics of solar cells	48
19	Simulation of a spectrally flat optical spectrum.	49
20	Simulation of a AM0 and AM1.5G solar spectrum.	50

21	Simulation of a summer and winter spectrum measured outdoors in Stuttgart.	52
22	IV-characteristics of a triple-junction solar cell for different spectra.	54
23	IV-characteristics of a triple-junction solar cell under no illumination.	55
24	Reflection efficiencies for used coatings.	68

1 Introduction

Multi-junction solar cells push the cell efficiency beyond the detailed balance limit¹. Thermalization losses are reduced by utilizing different spectral parts in the individual subcells². So far, even tandem solar cells have overcome the detailed balance limit³ while triple-junction cells reach efficiencies exceeding 40%^{4–6} (AM1.5D). Solar cells with even more junctions are expected to overcome the 50% benchmark^{7,8}.

While high efficiency multi-junction solar cells are widely used in space applications under constant spectral conditions⁹, their use under varying terrestrial spectra^{10,11} causes efficiency fluctuations of up to $\pm 15\%$ ¹² since the performance in series connection is limited by the worst performing cell^{13,14}. Optimization of such multi-junction solar cells, i.e. matching the currents of the individual subcells, is performed under laboratory conditions with a simulated AM1.5 spectrum⁸. This is a problem for reliable outdoor-performance predictions of solar cells since spatiotemporal spectral variations are not taken into consideration¹⁵. To overcome this problem meteorological models have been developed which provide spatially and temporally resolved irradiance distribution forecasts in a broad geographical range¹⁶.

Generally, a reproducible and precise simulation of a broadband solar spectrum and its dependence on environmental conditions is needed to experimentally verify efficiency variations of solar cells due to varying spectra. Such simulations are difficult to achieve with currently existing lamp- or LED-based solar simulators, that use a sequence of optical filters or spectrally selective mirrors to shape the spectrum from one or a combination of these light sources, for the following reasons:

(i) Since optical filters absorb in a relatively large spectral region, they cannot individually address small wavelength intervals of just a few nanometers and no lamp type offers a spectrum sufficiently close to the solar one¹⁷. This results in deviations from the desired spectrum that can in turn corrupt the current-match

and thus the efficiency when operating a multi-junction solar cell under real and thus deviating conditions¹⁸.

(ii) These devices have a limited feasibility for accounting for natural variations of a spectrum since filters have to be replaced.

The device performance of some currently existing solar simulators is cited^{14,18–20}. This evidently means that new optical devices which can generate essentially arbitrary broadband optical spectra with high precision are needed to experimentally study spectral effects on the efficiency of multi-junction solar cells. In this thesis, a broadband laser based solar simulator comprising a supercontinuum white light fiber source (WLS) and a symmetric 4-f optical synthesizer with a broadband spatial light modulator described and demonstrated. The WLS's spectrally integrated power is 4 W before²¹ and 0.15 W after the setup at maximum transmission. Various spectra are simulated, e.g. a flat wavelength spectrum as well as an AM0 and an AM1.5G spectrum in the range from 480 nm to 1600 nm showing the feasibility of this setup as a solar simulator with a significantly improved spectral match compared to existing solar simulators. Since the setup can generate essentially arbitrary spectra in the given range it allows for versatile testing schemes such as simulating the spectral variations measured outdoors.

The concept of multi-junction solar cells is introduced in the first section – along with a brief investigation of spatiotemporal variations of the solar spectrum and their influence on high efficiency solar cells. The second section is devoted to introducing spatial light modulators as well as discussing the theoretical background of the optical modulation within them. In the third section the design of the experimental setup – the optical synthesizer – is presented, where emphasis is placed on the selection of the individual components. The fourth section deals with the calibration of the optical synthesizer. This calibration is the basis for the fifth section that makes use of these results for the derivation of an algorithm being able to generate essentially arbitrary spectra. The remainder of

that section is then showing the experimentally generated spectra. Furthermore a triple-junction solar cell is tested under different spectra to prove the feasibility of the setup as a solar simulator. The final section shows up the limits of the setup as well as summarizes its advantages and disadvantages and gives some prospects for the future.

2 Some aspects of photovoltaic energy conversion

2.1 Multi-junction solar cells

A short introduction is given to the influence of the spectral distribution of the incident light on the efficiency η of a solar cell, where η is defined as the quotient of light power P_{in} incident on the solar cell and the power P the solar cell can deliver. Almost all photons with an energy $E_{ph} = h\nu$ equal to or exceeding the bandgap E_g are absorbed and those with $E_{ph} < E_g$ are transmitted in an ideal single-junction solar cell.

Photon absorption leads to a generation of an electron-hole-pair with the energy of the charge carriers being exclusively determined by the bandgap and the photon energy (cp. Fig. 1). Rapidly, these charge carriers are thermalized, i.e. the energy levels of all charge carriers generated in this way can be described by a Fermi-Dirac distribution at some temperature (much higher than room-temperature).

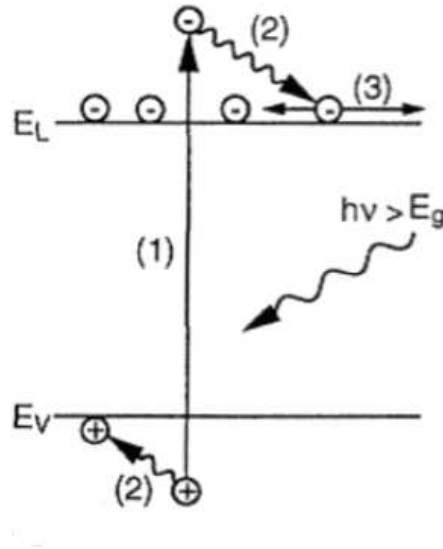


Figure 1: Illustration of thermalization losses in a semiconductor with E_V being the upper end of the valence band and E_L the lower end of the conduction band. A photon at an energy $E_{ph} > E_g = E_L - E_V$ is absorbed and generates an electron-hole-pair (1). The fraction of the photon energy exceeding E_g is rapidly converted to lattice vibrations (phonons) on a picosecond time scale. After this thermalization process (2), the charge carriers can diffuse through the semiconductor (3)²².

According to this distribution, most charge carriers are very close to the lower end of the conduction band. In turn, most of the excess energy $E_{ph} - E_g$ of photons with $E_{ph} > E_g$ cannot be converted to electrical energy. Obviously, the energy of the transmitted photons cannot contribute to photovoltaic energy conversion either²³.

From this point of view, the ideal spectrum for such a solar cell is monochromatic with $E_{ph} = E_g$. The utilization of broadband optical spectra, like the solar one, demands for an optimization of the trade-off between thermalization and transmission losses by finding the ideal bandgap. This ideal value is found to be $\approx 1.4 \text{ eV}$ ²⁴ for a single pn-junction solar cell under terrestrial AM1.5G spectra. The efficiency can be increased significantly by using more than one junction²⁵. These multi-junction solar cells are composed of a stack structure of single-junction solar cells (subcells), electrically connected in series²⁶. Fig. 2 illustrates this for a InGaP/InGaAs/Ge triple-junction solar cell.

The top cell in this stack has the highest bandgap and (ideally) absorbs all high energy photons (here: violet) with an energy exceeding this bandgap energy. All subsequent subcells have a decreasing bandgap and in turn absorb the high energy fraction of the remaining spectrum (here: green and red). The key advantage of such multi-junction solar cells is the narrower bandwidth in each subcell allowing for a much better trade-off between thermalization and transmission losses. In turn, this increases the possible efficiency of the cell.

The open circuit voltage V_{OC} is given by the sum of the open circuit voltages of the individual subcells ($V_{OC,i}$)²⁷, as given by Eq. 1.

$$V_{OC} = \sum_i V_{OC,i} \quad (1)$$

While this value is essentially independent of the incident spectrum, the short circuit current I_{SC} is very sensitive to it. Neglecting all loss mechanisms apart from those mentioned above, all absorbed photons contribute to I_{SC} in a single-junction solar cell. The same holds true for the *possible* I_{SC} in each subcell of

a multi-junction solar cell, but the resulting I_{SC} is limited by the subcell with the fewest absorbed photons due to the series connection. In turn, the efficiency of a multi-junction solar cell is limited by the worst performing subcell. Thus, efficiency maximization demands for the *possible* currents in all subcells to be equal. This condition is called current-matched.

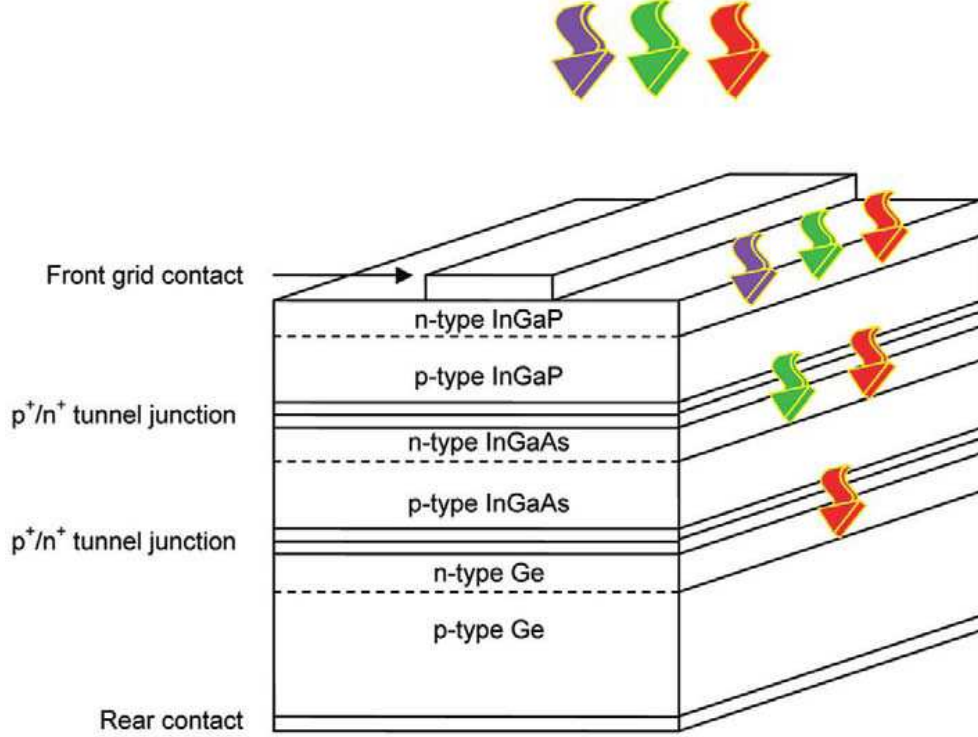


Figure 2: Stack structure of a InGaP/InGaAs/Ge triple-junction solar cell. A front contact grid and a rear contact make up the terminals of the cell. The remaining stack comprises three single pn-junction solar cells with decreasing bandgap from top to bottom, electrically connected in series by heavily doped tunnel junctions. The high energy photons (violet) of a broadband optical spectrum are absorbed in the top cell. The middle cell is in turn illuminated by intermediate (green) and low (red) energy photons. The first ones are absorbed in the middle cell while the remaining photons are transmitted to the bottom cell that absorbs most of the remaining photons²⁸.

The relation between the current through a solar cell and the voltage across its terminals is called IV-characteristic. An example for the IV-characteristic of a single pn-junction solar cell is given in Fig. 3, where the current has been replaced by the current density J

$$J = \frac{I}{A}, \quad (2)$$

with A being the area of the solar cell. The black curve shows the (exponential^{1,29}) characteristic for the unilluminated cell and the red curve for the illuminated cell^a, according to Eq. 3

$$J = J_0 \left(e^{\frac{eV}{kT}} - 1 \right) - J_{SC}, \quad (3)$$

where J_0 is the saturation current density, e the elementary charge, V the voltage across the terminals of the solar cell, k the Boltzmann constant and T the temperature.

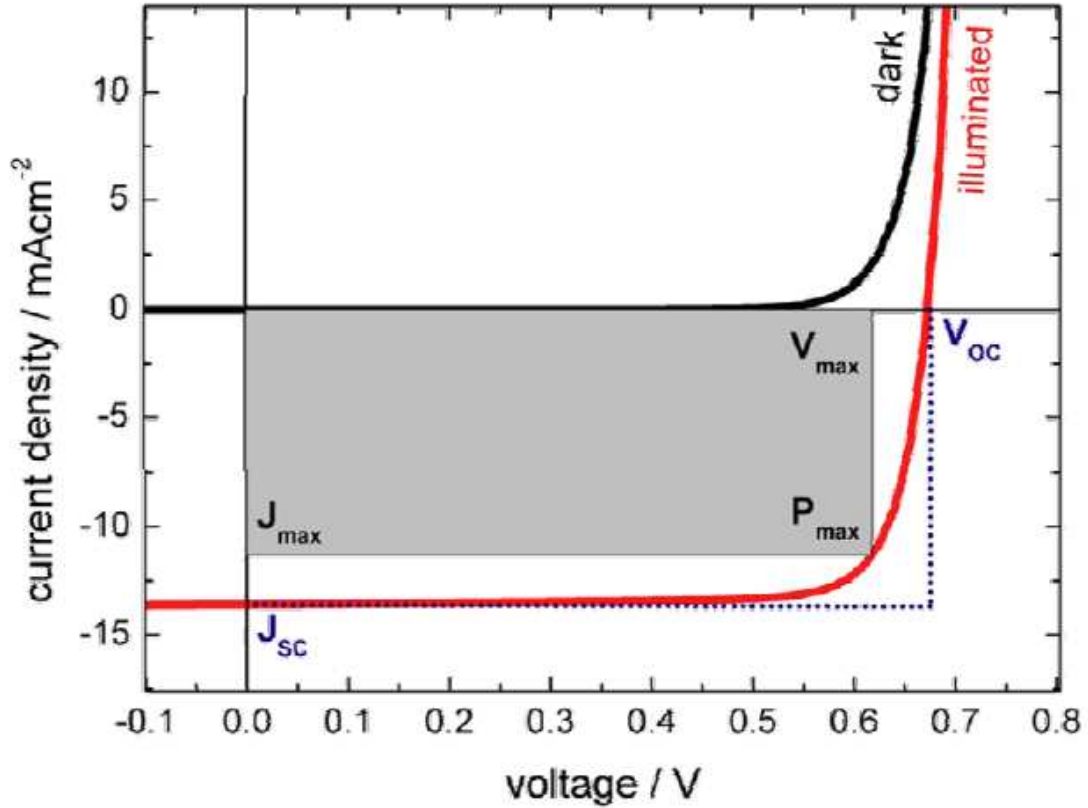


Figure 3: Current-voltage characteristic of a single pn-junction. Unilluminated junction (dark curve) has an exponential characteristic and the illuminated junction (red curve) a shifted exponential characteristic. The intersection of the red curve with the current axis is called short circuit current density J_{SC} and the intersection with the voltage axis open circuit voltage V_{OC} . The pair of values J_{max} and V_{max} having a maximum product describe the state of operation delivering the maximum possible power P_{max} ³⁰.

^aNo systematic analysis has been performed for (especially non current-matched) multi-junction solar cells so far.

Besides the previously mentioned optimization when seeking to extract the maximum possible power P_{max} out of a solar cell, a second aspect has to be considered. A solar cell delivers the power P according to

$$P = JAV = IV, \quad (4)$$

where I is the current through the cell and V the voltage across its terminals. The pair of values (J_{max} and V_{max}) on the IV-characteristic with a maximum product allows for the maximum possible power to be extracted out of the solar cell. This state of operation is also called the maximum power point. Fig. 3 illustrates it by a gray rectangle with a maximized area.

Interested readers are referred to^{31–33} for more information on solid state physics and the structure of a single-junction solar cell as well as the mechanism for the conversion of solar to electrical energy.

2.2 The solar spectrum

The spectrum coming from the sun is approximately a blackbody spectrum at $T = 5780\text{ K}$ ³⁴ before passing through the atmosphere of the earth. On the way through it, the spectrum can change significantly³⁵. One reason is the absorption by atmospheric gases and Rayleigh scattering at gases or dust/dirt is another one. Light with short wavelengths is scattered stronger than low energy light³⁶. This effect is so strong that it is even visible to the naked eye, e.g. the red sunsets and the blue sky. Also the amount of clouds covering the sky has an influence on the solar spectrum³⁷.

All these factors can change the solar spectrum significantly, but the key problem is that these changes are neither constant in time nor space³⁴ (location on earth). The major contribution is the changing amount of air the sunlight has to pass through¹⁵. This amount of air is called air mass (AM) and is given in units of one atmospherical thickness. The initial spectrum (in space) is thus called AM0 spectrum since the light has to pass through the atmosphere zero times. Accordingly there exist AM1.0 and AM1.5 spectra. The latter one is frequently taken as a reference spectrum for solar cells since the light has to effectively pass through 1.5 atmospheres in average over the day before reaching the surface of the earth. There is even a further designator for the AM1.5 spectrum. One distinguishes in between global and direct spectra for spectra with (AM1.5G) and without (AM1.5D) contributions from scattered light.

In summary, there is nothing like *the* solar spectrum. Fig. 4 gives an example of how strong these variations can be. It compares the AM1.5G reference spectrum to three spectra measured in Loughborough at different times³⁸. The average photon energy (APE), being a measure for the blueshift of a solar spectrum, changes significantly in time.

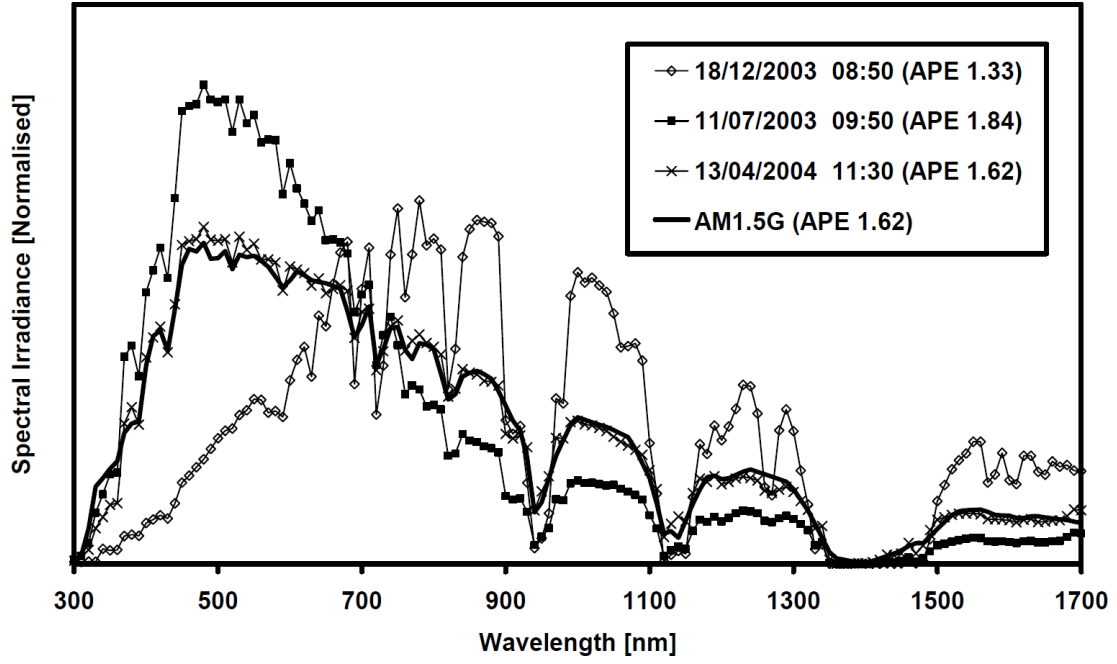


Figure 4: Examples for temporal variations of the solar spectrum in Loughborough³⁸ in comparison to the AM1.5G reference spectrum (bold solid line). Changes in the spectrum affect the average photon energy (APE), too.

3 Spatial light modulators

3.1 Functional principle of a spatial light modulator (SLM)

A spatial light modulator is an electronically addressable waveplate harnessing modulation of amplitude as well as phase of a linearly polarized monochromatic light wave focused into it^{39,40}. This section is dedicated to elucidating its functional principle. The heart of the SLM is a twisted nematic liquid crystal display (LCD) as shown in Fig. 5.

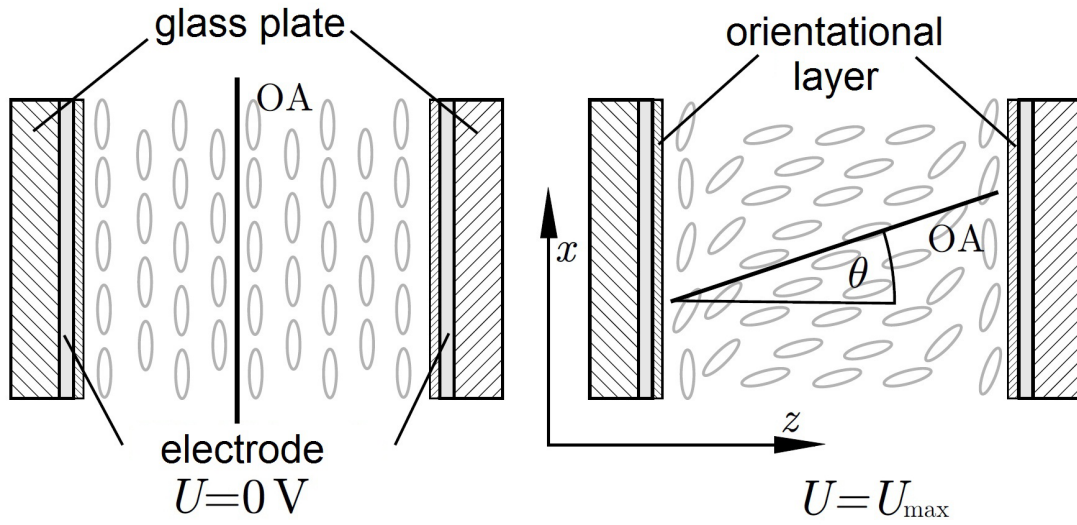


Figure 5: Structure of one pixel in a twisted nematic liquid crystal display-spatial light modulator (LCD-SLM, CRi SLM-640-D): Zero electric field (left) and maximum electric field (right), depending on the applied potential difference U in the range from zero to U_{max} . The space in between two stacks consisting of a glass plate, an electrode and an orientational layer is occupied by birefringent liquid crystals with a nonzero electric dipole moment along their optical axis (OA). In zero electric field all crystals align in parallel – governed by the orientational layer (left). When increasing the field the bulk crystals make an angle θ with the propagation direction of the light (z -axis)⁴¹.

The liquid crystals occupy the space between two stacks consisting of a glass plate, an electrode and an orientational layer⁴². The cigar-shaped crystals that have a nonvanishing electric dipole moment \vec{p} preferably align along this layer and in parallel to their neighbors. All liquid crystals are oriented in parallel to each other as shown in the left part of Fig. 5 assuming that no potential difference is applied to the two electrodes.

When increasing the voltage, an electric field in between the two electrodes builds up and the dielectric in between is polarized according to Eq. 5

$$\vec{P} = \epsilon_0 \chi \vec{E}, \quad (5)$$

where P is the polarization, ϵ_0 the vacuum permittivity, χ the susceptibility tensor and \vec{E} the total electric field inside the dielectric. The total field \vec{E} is the vector sum of \vec{E}_0 that would be present in the absence of any dielectric and the polarization field, according to Eq. 6.

$$\vec{E} = \vec{E}_0 + \frac{1}{\epsilon_0} \vec{P} \quad (6)$$

Now this electric field exerts a torque \vec{N} on the dipoles, as given by Eq. 7, tending to align the crystals along the field lines.

$$\vec{N} = \vec{p} \times \vec{E} \quad (7)$$

This effect is strongest in the center of the cell and almost compensated in the proximity of the orientational layer. A trade-off between both situations is established in intermediate regions, as illustrated in the right part of Fig. 5.

The liquid crystals show a positive uniaxial birefringence, i.e. they have a larger extraordinary than ordinary index of refraction ($n_e > n_o$)⁴³, with the optical axis being the long crystal axis. This results in a vanishing birefringence in the limit of high voltages and maximum birefringence at zero potential difference, both for light propagating in the z-direction. Thus the extraordinary index of refraction reaches its maximum value at zero applied voltage resulting in a maximum phase shift and vice versa. This effect can be exploited to control the phase of an electromagnetic wave polarized along the x-direction. Furthermore an array of such elements (pixels), in the following called mask, can be used to modulate non-monochromatic light by imaging small wavelength intervals into different pixels (hence the adjunct spatial).

Next, this phase shifting is illustrated on the basis of data measured by the manufacturer of the SLM (CRI) with their own single-mask SLM (NM-type, i.e. optimized for the infrared spectral range by using thicker LCD-pixels). Voltages between 0 V and 10 V can be applied at 12 bit resolution, which results in 2.44 mV per bit. This voltage is encoded by an integer number called bit-value. When increasing this bit-value from zero to its maximum of 4095 the liquid crystals align more and more along the propagation direction of the incident light. This decreases the extraordinary index of refraction and hence decreases the phase shift of the electric field component of the light in the respective direction (x-direction in Fig. 5). The typical dependence of the gained phase (modulation) on the applied bit-value is shown in Fig. 6.

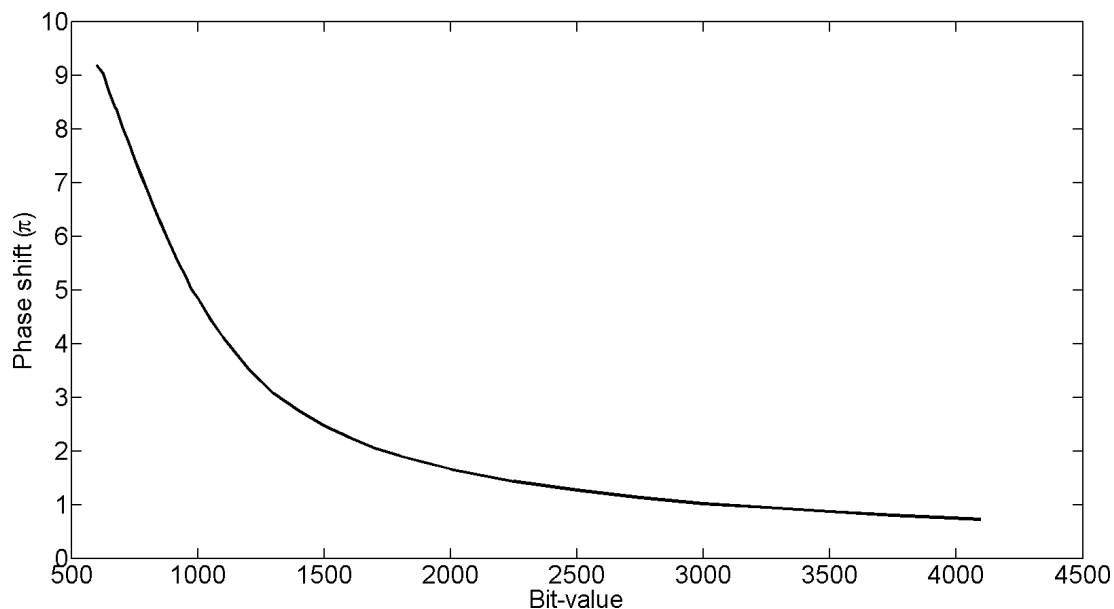


Figure 6: Reference modulation curve for a single mask SLM at $\lambda = 633$ nm (measured by the manufacturer with their single-mask SLM). The phase shift is plotted as a function of the applied bit-value, which encodes the voltage applied to the LCD-pixel [0,10] V at 12 bit resolution. The upper end of the plot range (4095) represents the maximum voltage.

The modulation changes significantly, i.e. by multiples of π , between 600 and 2000, while the remaining half of the addressable voltage range can change it by $\approx \pi$ only. Despite the large phase increase towards lower bit-values there is hardly any further change below 600⁴⁴.

It must be mentioned that this curve is valid for a wavelength of $\lambda = 633\text{ nm}$ only, but the dispersion can be compensated for by multiplying the curve in Fig. 6 by a constant factor, e.g. 1.33 for $\lambda = 400\text{ nm}$ and 0.88 for $\lambda = 1600\text{ nm}$. Going into more details is of no benefit since all SLMs are slightly different and require their own curves.

3.2 Amplitude modulation with a dual-mask SLM

Several SLM designs are available. One class is the single-mask SLM allowing for the modulation of either phase or amplitude. Another one is the dual-mask unit allowing for both. Although the planned experiments exclusively require an amplitude modulation of a given spectral energy current density per wavelength, for which a single-mask design would have been sufficient, the dual-mask unit is explained in more detail, because this is the kind of device that is used in the experiments.

The optical axes of the two masks in a dual-mask SLM are oriented at $\pm 45^\circ$ with respect to the polarization direction, as illustrated in Fig. 7. These directions are called \hat{e}_A for the direction of the optical axis of mask A and \hat{e}_B for the respective direction of mask B, as given by Eq. 8.

$$\hat{e}_{A,B} = \frac{1}{\sqrt{2}}(\hat{e}_x \mp \hat{e}_y) \quad (8)$$

In the following, the amplitude modulation is discussed in detail, starting with an incoming electromagnetic wave, as given by Eq. 9,

$$\vec{E}_{in} = E_0 \cos(kz - \omega t) \hat{e}_x \quad (9)$$

where E_0 is the amplitude of the incoming field, k the magnitude of its wavevector and ω the angular frequency. For a formal description, electric field components along the optical axes have to be dealt with. Therefore it is convenient to change coordinates from the (x,y,z)- to the (A,B,z)-system introduced in Eq. 8.

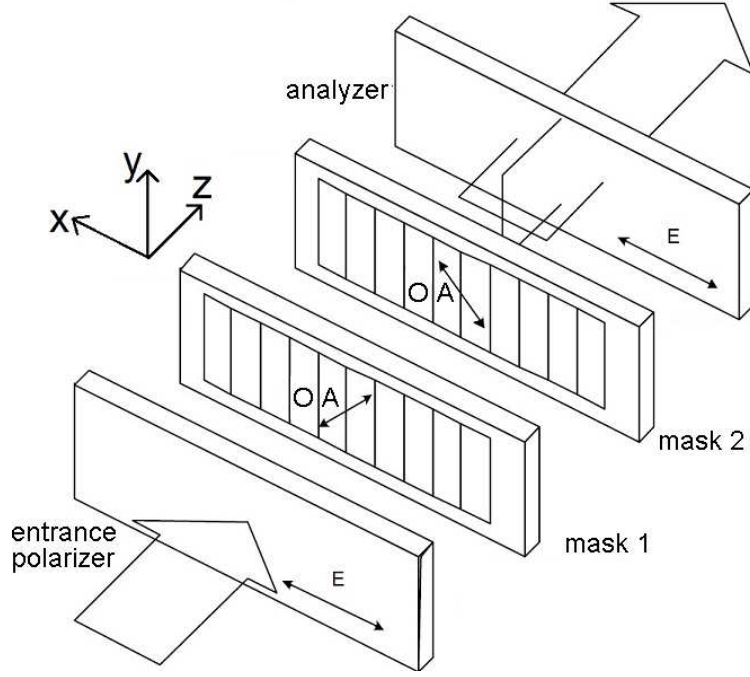


Figure 7: Mask alignment in a dual-mask SLM: The incident light is linearly polarized by the entrance polarizer and then passing through the two masks. Their optical axes (OA) are oriented at $\pm 45^\circ$ with respect to the polarization direction E , harnessing the modulation of phase as well as amplitude. Finally the retarded and generally elliptically polarized light passes the analyzer that selects the horizontally polarized component. The pixel pitch is $100 \mu\text{m}$ and the two masks are 1 mm apart.

Using these coordinates, the incoming electric field components in these directions are given by Equations 10 and 11.

$$\vec{E}_{in,A} = \frac{E_0}{\sqrt{2}} \cos(kz - \omega t) \hat{e}_A \quad (10)$$

$$\vec{E}_{in,B} = \frac{E_0}{\sqrt{2}} \cos(kz - \omega t) \hat{e}_B \quad (11)$$

When the same voltage is applied to both masks, the two orthogonal electric field components of the light (A and B) are equally retarded. This results in a pure phase modulation leaving the polarization state unchanged. For a different modulation in the respective masks the gained phase equals the average retardance of the waves A and B⁴⁵. Since an equal retardance in both masks has no effect on the polarization state, only the differential retardance φ can affect it.

After passing both masks, the modulated electric field is given by Equations 12 and 13

$$\vec{E}_{mod,A} = \frac{E_0}{\sqrt{2}} \cos(kz - \omega t + \varphi) \hat{e}_A \quad (12)$$

$$\vec{E}_{mod,B} = \frac{E_0}{\sqrt{2}} \cos(kz - \omega t) \hat{e}_B, \quad (13)$$

where an overall phase shift common to both waves is suppressed. The differential retardance φ is responsible for the amplitude modulation. This can be shown by deriving an expression for the transmitted wave. For this purpose, the modulated field is evaluated in the original coordinate system by Eq. 14.

$$\vec{E}_{mod} = \begin{pmatrix} E_{mod,A} \cos(45^\circ) + E_{mod,B} \cos(45^\circ) \\ E_{mod,B} \sin(45^\circ) - E_{mod,A} \sin(45^\circ) \\ 0 \end{pmatrix} = \frac{1}{\sqrt{2}} \begin{pmatrix} E_{mod,A} + E_{mod,B} \\ E_{mod,B} - E_{mod,A} \\ 0 \end{pmatrix} \quad (14)$$

An (ideal) analyzer selects the x-component of the modulated electric field, thus the transmitted amplitude is given by Eq. 15.

$$E_T = \frac{1}{\sqrt{2}} (E_{mod,A} + E_{mod,B}) = \frac{E_0}{2} (\cos(kz - \omega t + \varphi) + \cos(kz - \omega t)) \quad (15)$$

The intensity is defined by⁴⁶

$$I = \langle S \rangle_t = \left\langle |\vec{E} \times \vec{H}| \right\rangle_t = \left\langle \frac{|E|^2}{\mu_0 c} \right\rangle_t, \quad (16)$$

where S is the magnitude of the Poynting vector, H the magnetic field, μ_0 the vacuum permeability, c the speed of light and $\langle .. \rangle_t$ denotes the temporal average. Inserting Eq. 15 into 16 yields

$$\begin{aligned}
I_T &= \frac{E_0^2}{4\mu_0 c} \langle [\cos(kz - \omega t + \varphi) + \cos(kz - \omega t)]^2 \rangle_t \\
&= \frac{I_0}{2} \left[\underbrace{\langle \cos^2(kz - \omega t + \varphi) \rangle_t}_{\frac{1}{2}} + \underbrace{\langle \cos^2(kz - \omega t) \rangle_t}_{\frac{1}{2}} + 2 \langle \cos(kz - \omega t + \varphi) \cos(kz - \omega t) \rangle_t \right] \\
&= \frac{I_0}{2} [1 + 2 \langle \cos(kz - \omega t + \varphi) \cos(kz - \omega t) \rangle_t] \\
&= \frac{I_0}{2} [1 + \cos(\varphi)] .
\end{aligned} \tag{17}$$

The last step can be readily performed using a trigonometric identity, as shown in the appendix. I_0 is the intensity of the incoming wave. I_T shows the expected behaviour of remaining unchanged at zero differential retardance. Furthermore, Eq. 17 reveals that the transmitted intensity can be varied between 0 and I_0 at $\varphi = 0$ and π , respectively. This result is of central importance for the discussion in section 6.

4 Design of the experimental setup

4.1 Setup of an optical synthesizer

Controlling the amplitude of a monochromatic light wave focused into one single pixel of a dual-mask SLM was discussed in the last section. This scheme can be easily generalized to non-monochromatic light by splitting up the different spectral components of a collimated beam and focusing them into different pixels of the same mask. The optics performing this task in combination with the SLM is called an optical synthesizer (cp. Fig. 8) in analogy to acoustics, where the amplitude of different sound frequencies can be adjusted to a desired value in an acoustic synthesizer.

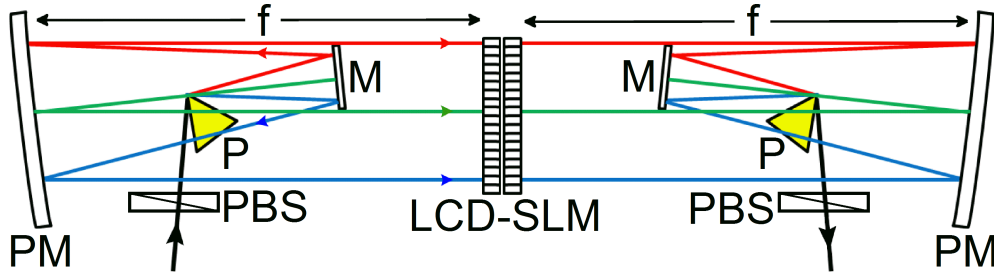


Figure 8: Schematic of the experimental setup. Radiation from a coherent broadband supercontinuum white light source (extending from 480 - 2300 nm) is expanded and collimated to a beam size of 8 mm. The beam is sent into a symmetric 4-f optical synthesizer, where it is horizontally polarized by a Glan-Laser polarizing beam splitter (PBS). It is then dispersed by a prism (P), deflected by a silver mirror (M) and focused by an $f = 445$ mm protected aluminium-coated parabolic mirror (PM) into a LCD-SLM to control the polarization state of each wavelength component. The beam is recollimated in a symmetric arrangement of mirrors, prism and polarizing beam splitter.

For dispersing the different colors a prism P is used instead of a grating because of its quite low diffraction efficiency compared to the transmission of a prism. This is required for keeping the possible output power behind the synthesizer as large as possible. All the different colors could be focused by a lens into their respective pixels, too, but this would introduce chromatic aberration. For this reason, a parabolic mirror PM (focal length f) is used even though this design raises a geometric problem: The prism as well as the SLM have to be at a distance f from the mirror and should both be on its optical axis, which is impossible for obvious

reasons. One compromise would be arranging prism and SLM next to each other, but this induces aberration due to the large off-axis angle. This problem can be solved by placing a flat mirror M in between the parabolic mirror and the SLM such that the upper edge of the flat mirror is slightly below the optical path from the PM to the SLM.

The right half of the optical synthesizer is symmetric to the left one and responsible for recombining all the spectral components to a collimated beam. The polarizers provided by the manufacturer of the SLM are not used because of their limited spectral range. These polarizers would have been located directly in front of and after the SLM, as illustrated by Fig. 6. Instead, two Glan Laser GL10 polarizing beam splitters (PBS) with a free spectral range from 350 nm to $2.3\text{ }\mu\text{m}$ ⁴⁷ are placed in front of the first and after the second prism. Both polarizers are horizontally oriented. Although the optical modulation could be performed using any of the four possible combinations (both horizontal/vertical or one vertical and the other one horizontal), the output power is maximized by aligning both PBS horizontally since the prism is approximately in the Brewster angle and by this reflection losses at both prisms can be minimized.

4.2 Selection of the components

4.2.1 Mirror selection

Before describing the selection criteria for the used mirrors, a summary is given of all components that are decided at this stage. The first one is the WLS (Fianium SC-450-4) that generates a randomly polarized 4 W broadband supercontinuum (Fig. 9) extending from 450 nm to beyond $2\text{ }\mu\text{m}$ at a spectral power density of more than 2 mW/nm, a pulse duration of 5 ps and a pulse repetition rate of 40 MHz²¹. The second component is the polarizer (GL10), as described in the previous subsection and the last one is the dual-mask (twisted nematic) LCD-SLM (CRI, SLM-640-D). This type is used for its best IR-performance compared

to Jenoptik and Holoeye. The choice of a SLM determines the necessary focal plane of the optical synthesizer. The remaining free parameters are the prism material and the focal length of the mirror as well as its coating.

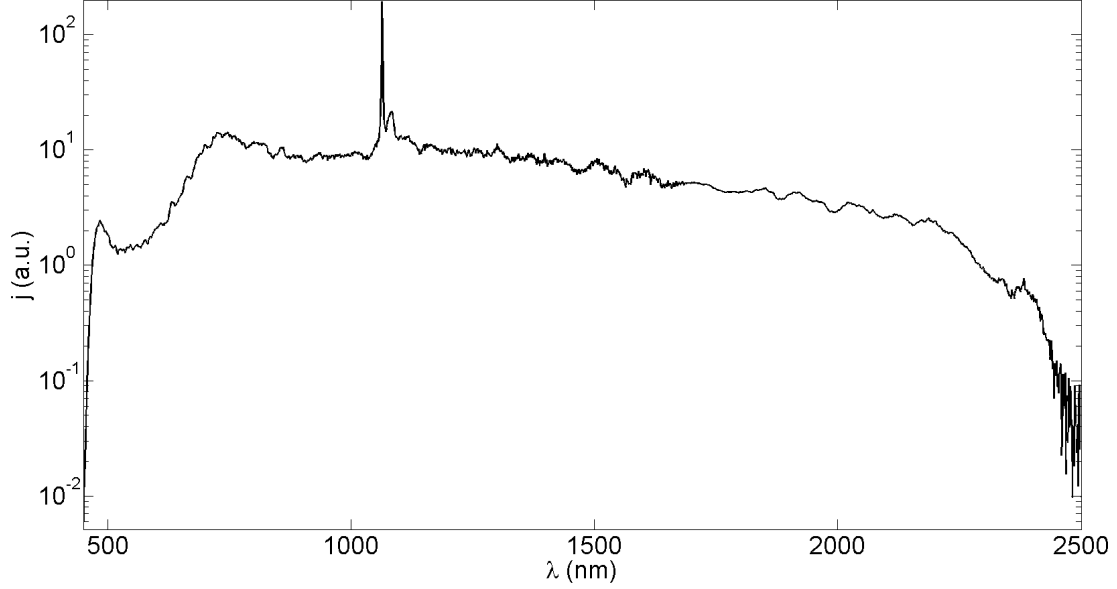


Figure 9: Spectrum of the white light source before passing through the optical synthesizer. The spectrally integrated average power is 4 W at a spectral power density of more than 2 mW/nm, a pulse duration of 5 ps and a pulse repetition rate of 40 MHz. The spectrum possesses a peak at 1060 nm due to the Yb-based pump laser.

Given the width of the LCD-panel (64 mm), a suitable focal length-prism combination has to be found allowing for all colors to be mapped into the LCD-SLM in parallel, as illustrated by Fig. 8, with the longest and shortest wavelength on the respective edges. The problem is tackled by first choosing a mirror since there are only a few different focal lengths available. A short focal length requires large off-axis angles θ and thus induces coma, while a longer focal length results in a larger beam focus' waist radius w_0 . A focal length of $f=445$ mm is chosen resulting in

$$\theta = \arctan \frac{\text{width}(LCD)/2}{f} = \arctan \frac{32 \text{ mm}}{445 \text{ mm}} = 4.1^\circ$$

and

$$w_0 = 0.637 \cdot \frac{\lambda \cdot f}{\text{beam diameter}} = 0.637 \cdot \frac{2.325 \mu\text{m} \cdot 445 \text{ mm}}{7 \text{ mm}} = 94 \mu\text{m}$$

for the longest wavelength $\lambda = 2325 \text{ nm}$, decreasing for shorter ones. Beam profile measurements disclose an approximately Gaussian beam profile at a $1/e^2$ diameter of 7 mm . $2w_0$ has to be compared to the pixel size of $\approx 100 \mu\text{m}$. Thus, the longest wavelengths cannot be focused into one pixel only. The ideal situation would be $2w_0 < 100 \mu\text{m}$ for all λ , but this small overlap is still a tolerable trade-off since neither the off-axis angle nor the beam diameter should be increased any further.

Two material types are possible for the coating: Protected aluminium and protected silver. Protected silver would be slightly better for the blue end of the spectrum⁴⁸, but the available mirrors were most commonly coated with protected aluminium or gold and the slightly improved performance of a silver mirror does not justify the extra costs for an individual coating.

4.2.2 Raytracing

For visualizing the previously mentioned imaging a ray tracing method is applied for the path from the first prism in Fig. 8 via the left PM to the LCD-SLM. As a simplification, the flat mirror M is omitted – ignoring not being able to put the prism as well as the SLM in the same place.

First, a relation between an incoming ray and its reflected ray at an arbitrary parabolic mirror of focal length f has to be found. Later on, f will be set to 445 mm for the visualization. The incoming ray may hit the mirror at an arbitrary position and angle. An incoming ray

$$x(y) = x_P + \frac{y_P - y}{\tan \varphi_i} \quad (18)$$

at an angle φ_i (i for incoming) through the prism located in $[x_P, y_P]$ is reflected in $[x_S, y_S]$ on the parabolic mirror

$$x(y) = a \cdot y^2, \quad (19)$$

where a is related to the focal length by $a = (4 \cdot f)^{-1}$. The point of intersection^b is readily calculated by equating Equations 18 and 19, yielding

$$y_S = -\frac{1}{2a \tan \varphi_i} + \sqrt{\frac{1}{(2a \tan \varphi_i)^2} + \frac{x_P}{a} + \frac{y_P}{a \tan \varphi_i}} \quad (20)$$

and

$$x_S = a \cdot y_S^2. \quad (21)$$

Inspection of Fig. 10 reveals that the negative of the outgoing angle φ_r is the alternate angle to $\varphi_i - 2\alpha$. The sum of all angles in a triangle equals 180° , such that

$$180^\circ = 90^\circ + \varphi_i + (90^\circ - \gamma - \alpha) \quad (22)$$

$$\Rightarrow \alpha = \varphi_i - \gamma, \quad (23)$$

which directly leads to

$$\varphi_r = \varphi_i - 2 \arctan(2a y_S), \quad (24)$$

where the relationship in Eq. 25 is used.

$$\tan \gamma = \frac{d}{dy} x(y) \quad (25)$$

Knowing φ_r and the point of intersection, an equation for the reflected ray can be found

$$y(x) = y_S + (x - x_S) \tan \varphi_r. \quad (26)$$

^bThe plus sign applies in Eq. 20 since the minus corresponds to the second (mathematically existent) intersection with an infinitely extended parabola.

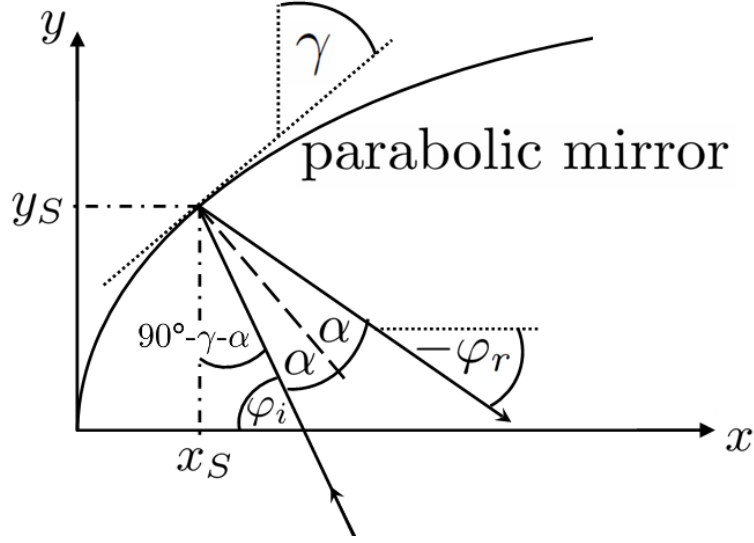


Figure 10: Reflection in the point $[x_S, y_S]$ of an incident light ray, making an angle of φ_i with the x-axis, on a parabolic mirror, at an angle of incidence α with respect to the surface normal (dashed line). The slope of the parabolic mirror in the point of intersection is parameterized by the angle γ affecting the angle $-\varphi_r$ that the reflected beam makes with the x-axis.

Having all the information that is needed, the tracks of the light rays can be visualized. While Fig. 8 represents the beams of different colors by one ray only concealing the beam diameter, this description is expanded to three rays now, a center one and two marginal rays. The implementation in MATLAB is given in the appendix and the result is shown in Fig. 11. Two beams, a blue one representing the 480 nm beam and a red one for 2325 nm originate at the prism (not shown) that would have had to be placed in the LCD in this plot. Both beams make an angle of $\pm 4.1^\circ$ with the horizontal, i.e. $\varphi_i = \pm 4.1^\circ$, resulting in an angle of 8.2° between the two outer beams. This angle is important for the choice of a suitable prism. The center rays are reflected at the parabolic mirror onto a horizontal track since the prism is located in the focal point of the mirror. The respective marginal rays are converging with the focal plane coinciding with the LCD-panel.

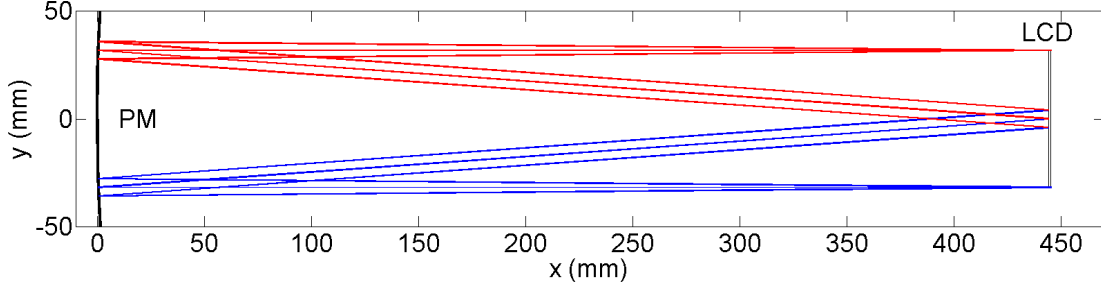


Figure 11: Figure generated by ray-tracing: Blue lines represent light rays with $\lambda = 480$ nm and the red ones alike for $\lambda = 2325$ nm. Each beam consists of three rays, the center one and two marginal rays. The two beams originate from a prism (not shown) that would have had to be placed in the liquid crystal display (LCD) in this plot. Both beams make an angle of $\pm 4.1^\circ$ with the horizontal resulting in an angle of 8.2° between them. The center rays are reflected at the $f = 445$ mm parabolic mirror (PM) onto a horizontal track since the prism is located in the mirrors focal point. The respective marginal rays are converging towards the center ones with the focal plane coinciding with the LCD-panel.

4.2.3 Raytracing for an off-axis mirror

The ray-tracing scheme derived above is used to check whether an off-axis parabolic mirror is a possible alternative to solve the geometric problem. A 90° $f = 245$ mm off-axis parabolic mirror is simulated with the two beams known from the last figure being incident on (Fig. 12). The center rays are again parallel to each other after the reflection, but a magnification of the focal plane reveals that it's tilted significantly. The x-coordinates of the marginal-beams' focal points are separated by 140 mm, which makes an effective modulation impossible since the spot size would exceed the pixel size by far for most wavelengths. This means that the off-axis mirror is no alternative to solve the geometric problem, but a flat mirror can be used, as shown in Fig.8.

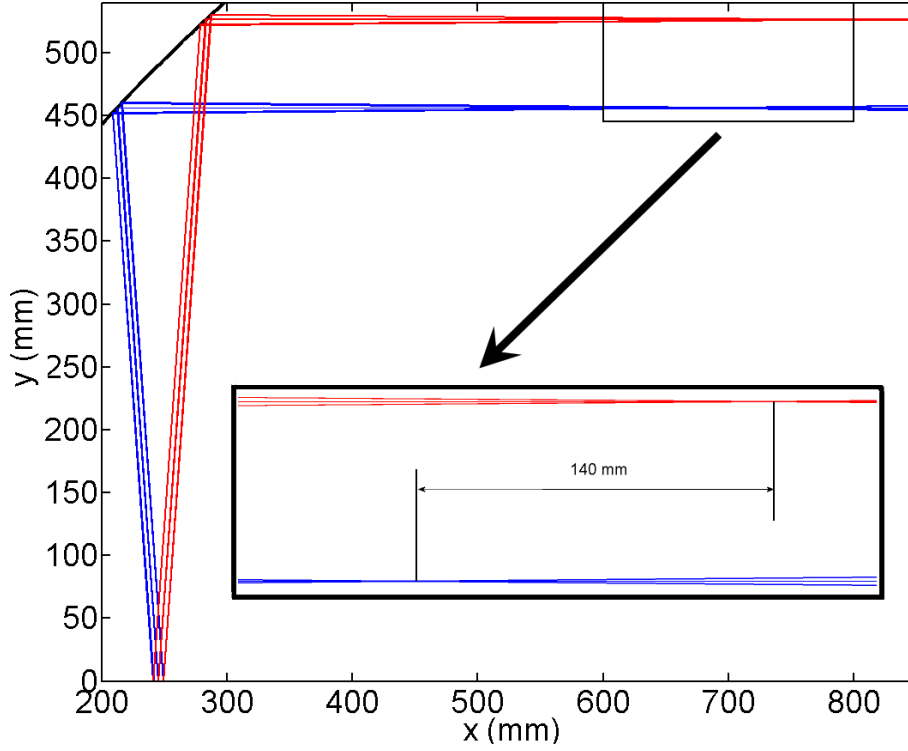


Figure 12: Two beams (the same ones as in Fig. 11) are incident on a $f = 245$ mm 90° off-axis parabolic mirror. The magnification of the focal plane reveals a focal point separation of 140 mm along the propagation direction.

4.2.4 Prism selection

Finally, it is shown how to choose a suitable prism for the mirror. For this purpose a material has to be picked, such that the equilateral (60°) prism generates an angle of 8.2° between the 480 nm and 2325 nm beam. Generally, the restriction to an opening angle of 60° is not needed, but a larger angle demands for a larger prism and the light rays inside the prism are closer to the critical angle for total internal reflection. In contrast to that a much smaller angle cannot provide a sufficient dispersive power. For this reason, the most commonly used opening angle of 60° is used. The deflection angle δ for this kind of prism is given by Eq. 27

$$\delta(\lambda) = \theta_i + \arcsin \left[\sin(60^\circ) \sqrt{n^2 - \sin^2(\theta_i)} - \sin(\theta_i) \cos(60^\circ) \right] - 60^\circ, \quad (27)$$

where n is the refractive index and θ_i the angle of incidence that is chosen to be the Brewster angle for 1060 nm to minimize reflection losses. The difference angle $\delta(480\text{ nm}) - \delta(2325\text{ nm})$ is plotted in Fig. 13 for all glass types in the SCHOTT database. The plot range is restricted for a better illustration of the relevant materials – thereby neglecting those being too far apart from the desired 8.2° line. Again, the code for the generation of this result is given in the appendix. Three material types are highlighted in the figure: N-LAF 36, N-LASF 44 and SF 4. SF 4 is chosen not only for being closest to the optimum, but for its higher transmission values, too.

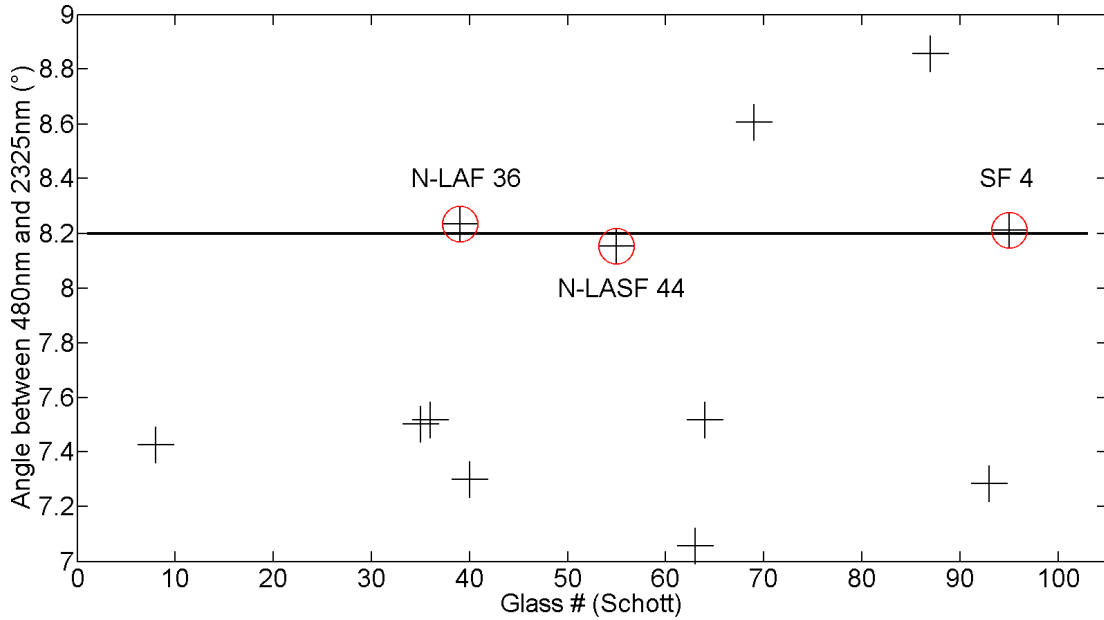


Figure 13: Calculated difference in deflection angle between light with $\lambda = 480\text{ nm}$ and $\lambda = 2325\text{ nm}$ dispersed by an equilateral 60° prism. The solid line at 8.2° represents the optimum for the optical synthesizer and the plus signs represent calculated values for different glass types given in the SCHOTT catalog, ordered by an arbitrary glass number. The three types being closest to the line are highlighted by red circles: N-LAF 36, N-LASF 44 and SF 4.

4.3 Summary of the experimental setup

A WLS generates a randomly polarized 4 W broadband supercontinuum extending from 450 nm to beyond $2\text{ }\mu\text{m}$. The converging^c output beam is collimated by a protected aluminium coated 3" parabolic on axis mirror with $f=445\text{ mm}$. The beam profile comprises a Gaussian mode and a surrounding hexagonal structure that is blocked by an 8 mm aperture.

The resulting beam enters the optical synthesizer (Fig. 8), where it is (horizontally) linearly polarized by a polarizing beam splitter and dispersed by a 60° SF 4 prism. The (silver coated) flat mirror is needed for minimizing the angle of incidence on the parabolic mirror that is placed a distance f behind the prism. All the different colors are focused into their respective pixels of the dual mask LCD-SLM by the parabolic mirror (again after its focal length f).

These pixels act as a 12 bit (values from 0 to 4095)^d programmable waveplate. Technically this is accomplished by applying maximum voltage to the second mask^e while decreasing the voltage from the maximum value (10 V) to a desired one for the first mask. This procedure introduces a phase modulation, too, which is of no interest here since the WLS has got long pulses (5 ps). One mask consists of 640 pixels at a pixel pitch of $100\text{ }\mu\text{m}$ resulting in a spectral resolution between 0.5 nm (VIS) and 8 nm (IR).

The right half of the setup is symmetric to the left part and recombines the different colors to a collimated beam. This beam passes the analyzer that discards the vertical polarization component and thus realizes the amplitude modulation. In this way, the optical synthesizer can individually reduce spectral components of just a few nanometer in bandwidth of an incident energy current density to the desired value in between the initial one and almost zero.

Fig. 14 shows the supercontinuum behind the synthesizer with the LCD-SLM set to maximum transmission for all wavelengths and thus gives the maximum values

^cCollimating optics in the fiber head.

^dThe resulting transmissions are nonequally spread.

^eThe second mask will be set like this in all the experiments.

the desired energy current density may take at each wavelength. The power is 0.15 W at an average spectral power density of $70 \mu\text{W}/\text{nm}$ and a minimum value of $18 \mu\text{W}/\text{nm}$. Approximately half of the incident power is lost when polarizing the beam, while the LCD transmits approximately 90%²¹ in the given modulation range. Towards the UV the performance is limited by the WLS and towards the IR by the onset of absorption of the LCD. At the time of this calculation this absorption was unknown, so the design will be optimized for the range from 480 nm to 2325 nm. This leaves about 80 pixels unused and in turn slightly reduces the possible resolution.

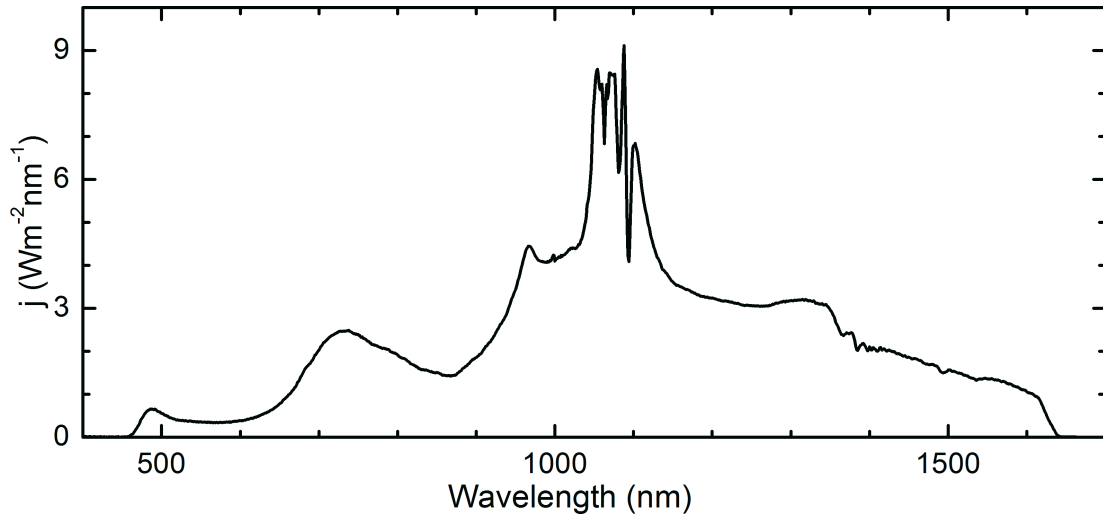


Figure 14: Spectrum of the white light source after passing through the optical synthesizer. The spectrally integrated average power of the exit beam is 0.15 W. The spectral peak at 1060 nm (cp. Fig. 9) is suppressed by placing a $125 \mu\text{m}$ thick gold wire directly behind the LCD-SLM. The long-wavelength cutoff at 1650 nm is due to the onset of absorption of the LCD display.

The original spectrum provided by the WLS possesses a peak at about 1060 nm (cp. Fig. 9) due to pumping of a nonlinear optical fiber that cannot be sufficiently suppressed by the amplitude modulation mentioned above. This problem is solved by placing a $125 \mu\text{m}$ thin gold wire at the respective position behind the LCD-SLM.

5 Calibration of the optical synthesizer

5.1 Wavelength to pixel-number mapping

The next step is calibrating the optical synthesizer. For manipulating the amplitude of a spectrum, it must be fixed which pixel of the SLM addresses which wavelength. To keep track of the pixels it's convenient to enumerate them from 1 to 640, starting from the long wavelength side of the SLM (upper end in Fig. 8). These numbers are simply called pixel-numbers. The relation between them and the wavelength being focused into this respective pixel can be found by evaluating the deflection angle $\delta(\lambda)$ (Eq. 27) of the SF 4 prism for all wavelengths. The wavelength-dependent index of refraction $n(\lambda)$ is computed using the Sellmeier-Equation (Eq. 28) for SF 4 glass with the coefficients⁴⁹ $B_1 = 1.61957826$, $B_2 = 0.339493189$, $B_3 = 1.02566931$, $C_1 = 0.0125502104$, $C_2 = 0.0544559822$ and $C_3 = 117.652222$

$$n(\lambda) = \sqrt{1 + \sum_{i=1}^3 \frac{B_i \lambda^2}{\lambda^2 - C_i^2}}, \quad (28)$$

where $[\lambda] = \mu\text{m}$. Inserting Eq. 28 into Eq. 27 yields a numeric relation for $\delta(\lambda)$ for all desired wavelengths. When subtracting the minimum angle, i.e. the angle $\delta(\lambda_{\max})$ for the maximum wavelength λ_{\max} considered in the calculation (it must be $\geq 2325 \text{ nm}$), from $\delta(\lambda)$, a difference angle $[\delta(\lambda) - \delta(\lambda_{\max})]$ is obtained. Using the rule of three the angles $[0^\circ, 8.2^\circ]$ can be converted to pixel-numbers $[1, 640]$. This is readily achieved by dividing the difference angle by the maximum possible angle (8.2°) and multiplying it by the maximum possible pixel-number (640). Hence the factor $\frac{640}{8.2^\circ}$. Now the pixel-number can be computed by Eq. 29

$$\text{pixel-number}(\lambda) = [\delta(\lambda) - \delta(\lambda_{\max})] \cdot \frac{640}{8.2^\circ} + \text{offset}, \quad (29)$$

where the offset accounts for the extended wavelength-range on the one hand (if $\lambda_{\max} > 2325 \text{ nm}$) and the lateral displacement of the SLM from the calculated reference position on the other hand. This reference position is the special po-

sition, where the 2325 nm are mapped into pixel 1 and 480 nm into pixel 640, respectively.

Eq. 29 is plotted in Fig. 15, with the black dashed line being the relation for $\lambda_{\max} = 2400$ nm and zero offset. This offset is experimentally determined by measuring the spectrum once with and without blocking pixel 320. This blocking is accomplished by setting pixel 320 in mask 1 to a bit-value of about 2000 while leaving all other pixels at a bit-value of 4095. The second spectrum will reveal a dip in intensity at the respective wavelength. Now the offset can be calculated by inserting these two values (320 as pixel-number and the measured wavelength) into Eq. 29, resulting in an offset of -76.4 . Taking it into account yields the green curve in Fig. 15. Following the same procedure for some other pixels (represented by the black circles in the figure) allows for checking and improving the mapping. This is accomplished by subtracting the linearly interpolated difference between the measured curve and the green one from the latter curve to get the final wavelength to pixel-number mapping (red curve).

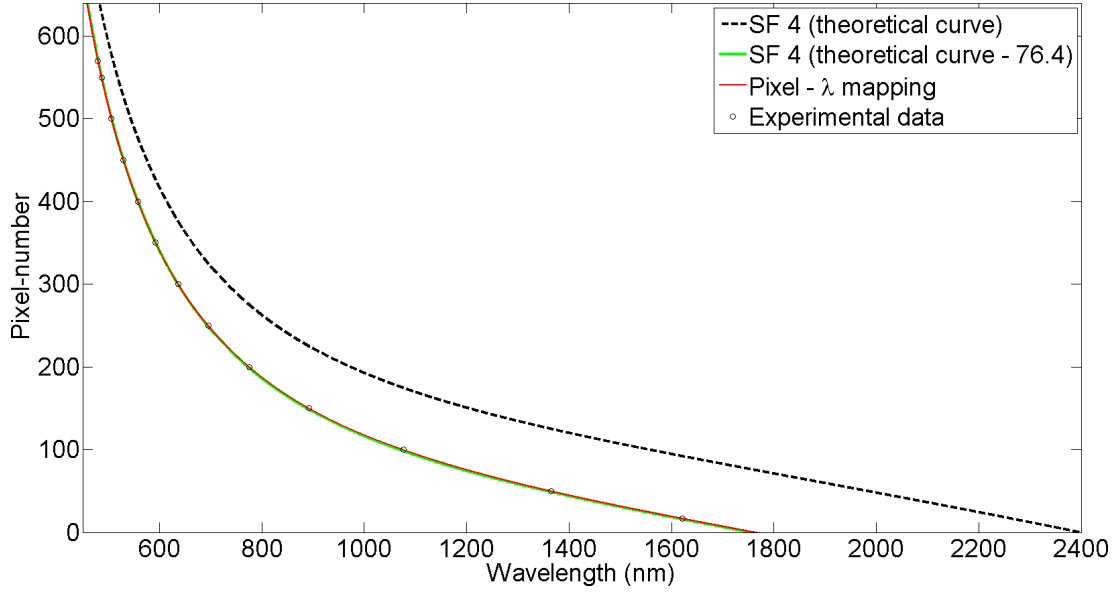


Figure 15: Mapping of wavelengths to pixel-numbers. The theoretical curve (black dashed line) in comparison to the experimental data (black circles). A constant offset is incorporated in the green solid curve. Small improvements to the latter one give the final mapping (red solid curve).

5.2 Minimum transmission spectrum by applying 'dark-bits'

An important step in the calibration procedure is the determination of the bit-values that produce minimum transmission when applied to the first mask for all wavelengths. This set of numbers is called darkbits. Unfortunately, all SLMs are slightly different such that the typical dispersion curve provided by the manufacturer cannot be used. For determining the darkbits a bit-value of 2000 is applied to the first mask before measuring the spectrum. The darkbit of the wavelength corresponding to minimum intensity in the spectrum is 2000. This procedure is repeated for different bit-values to cover the entire wavelength range. These values are represented by the red circles in Fig. 16 and can be reproduced by the fit model

$$\text{bit-value} = \frac{a}{\lambda} + b + c \cdot \lambda \quad (30)$$

with $a = (6.6 \pm 0.3) \cdot 10^5$, $b = 860 \pm 50$, $c = -0.08 \pm 0.03$ and $[\lambda] = \text{nm}$, which is the black solid line in Fig. 16. Correlating the wavelengths with the pixel-numbers using the mapping in Fig. 15 finally yields the darkbits.

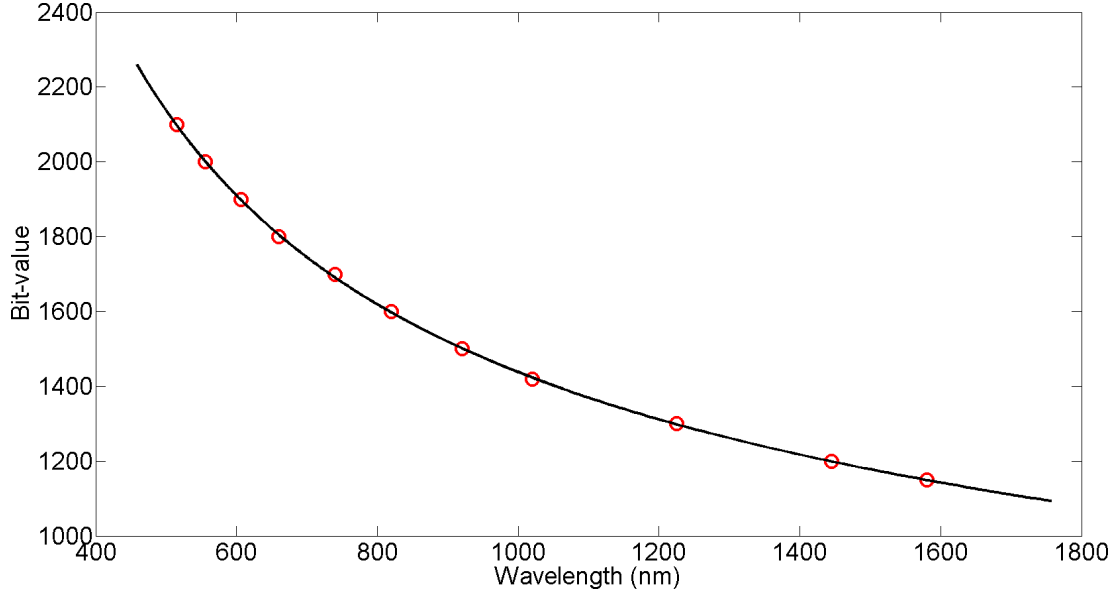


Figure 16: Bit-values producing minimum transmission (darkbits) as a function of the wavelength: Experimental data (red circles) in comparison to a fit as given by Eq. 30.

The suppression of I_{WLS} using these darkbits is better than two orders of magnitude, but the resulting 'dark' spectrum exhibits a nonzero intensity, to wit, even visible to the human eye. To give a rough estimate, the suppression of the full transmission spectrum exhibiting an intensity of 150 mW by $\gtrsim 2$ orders of magnitude leaves ≈ 1 mW of intensity.

6 Generation of arbitrary spectra

6.1 Calculation of bit-values for a desired spectrum

The starting point is the full transmission spectrum of the WLS (I_{WLS}), i.e. both masks being set to 4095. When seeking to convert it into an arbitrary spectrum (in the given range), the bit-values of the first mask have to be decreased (which increases the difference modulation) in order to decrease the transmitted intensity according to Eq. 17.

In the following, a scheme is derived for calculating the bit-values generating a desired spectrum. For this purpose, the reference modulation curve of Fig. 6 needs to be verified first. This can be accomplished by decreasing the bit-value of the first mask from 4095 and logging the values for the transmission minima and maxima at $\lambda = 633$ nm corresponding to phase shifts of odd and even multiples of π , respectively. Since the amplitude modulation is given by the difference of the modulations of the two masks, the minimum value corresponding to a bit-value of 4095 is subtracted from the curve, which then yields the phase shift of the extraordinary electric field component with respect to the ordinary one (referring to the optical axis of mask 1). This function is called difference modulation curve (DMC(b)), where b is an integer in the interval [0,4095]. From now on, the phase shift is given in multiples of π , i.e. $\text{DMC}(b) = 1$ means zero transmission.

Fig. 17 compares the reference (manufacturer's) DMC with our's. The difference can be compensated for by using a constant factor of 0.93 since the functional dependence is approximately the same. This is the key assumption that is used in the following calculation.

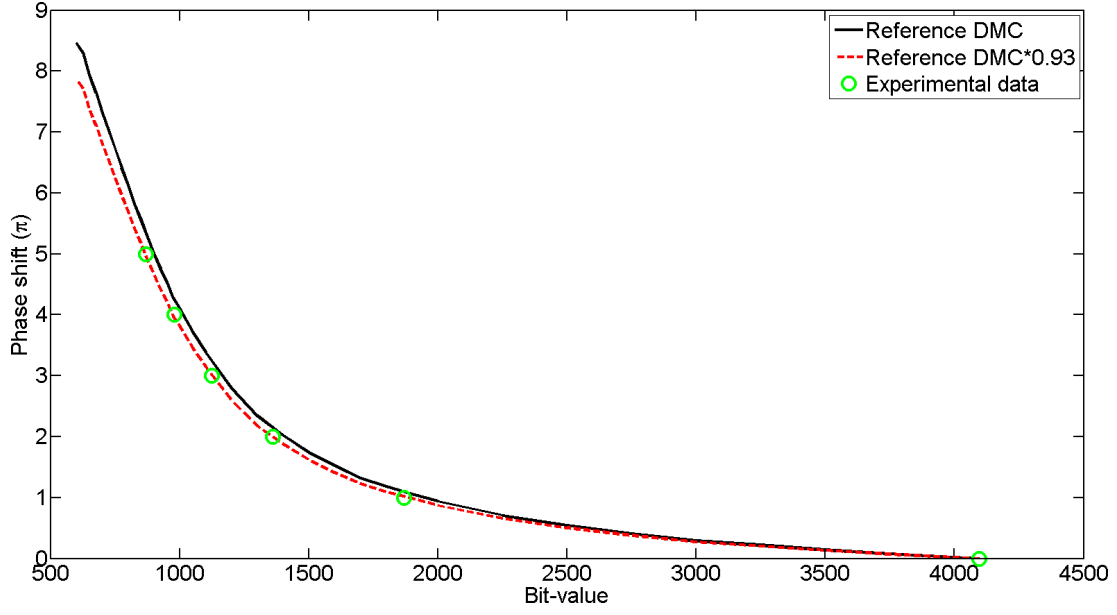


Figure 17: Difference modulation curve (DMC) for $\lambda = 633$ nm resulting from subtracting the minimum value (at a bit-value of 4095) of the modulation curve in Figure 6 from the curve itself. Reference curve⁴⁵ (solid black line) in comparison to some measured values (green circles) representing the respective transmission maxima and minima and the reference DMC times a constant factor of 0.93 (dashed red line), giving the best agreement with the experimental data.

Since the DMC is true for $\lambda = 633$ nm only, it is renormalized for each pixel according to Eq. 31 in order to take account for dispersion. This results in a set of 640 functions $DMC_p(b)$, where p is the pixel number.

$$DMC_p(b) = \frac{DMC(b)}{DMC(darkbits(p))} \quad (31)$$

The desired phase shift for each pixel φ_p can be computed by inverting Eq. 17:

$$\varphi_p = \cos^{-1} \left(2 \frac{I_T}{I_{WLS}} - 1 \right). \quad (32)$$

Please don't mix up φ_p and $DMC_p(b)$ – the first one being the function value of the second one at the bit-value \tilde{b} that is to be calculated, i.e.:

$$\varphi_p = DMC_p(\tilde{b}). \quad (33)$$

Inverting this relation yields

$$\tilde{b} = DMC_p^{-1}(\varphi_p). \quad (34)$$

Insertion of Equations 34 and 33 into Eq. 17 recovers the desired spectrum:

$$I_p(\tilde{b}) = \frac{I_{WLS}}{2} \left[1 + \cos \left(DMC_p(\tilde{b}) \right) \right]. \quad (35)$$

Summary

At this stage, all the steps that were necessary to arrive at the vector \tilde{b} are summarized. Eq. 34 demands for the phase shift φ_p and the inverse of the difference modulation curve DMC_p . The first one is readily determined when knowing the desired spectrum (I_T) and measuring the full transmission WLS spectrum (I_{WLS} , cp. Fig. 14) behind the synthesizer. The calculation of DMC_p is a bit more complex: First of all a relation between the pixel-numbers and the wavelengths being focused into these respective pixels has to be found. After this the dispersion in the SLM is analyzed by finding the bit-values necessary to produce a difference modulation of π (darkbits). These darkbits are necessary to renormalize the DMC for each wavelength, i.e. pixel. Now knowing this DMC_p , the inversion is done numerically.

6.2 Feedback loop

The bit-values that have been calculated using the procedure derived in the previous subsection should produce the desired spectrum. Unfortunately, this is only approximately true. The major contributions to the deviations are due to

- different variations in I_{WLS} for different wavelengths of the order of 10%.
- deviations of the calculated DMC_p from the actual function.
- a spectral overlap between pixels.

The first contribution could be minimized by measuring I_{WLS} directly before the calculation of \tilde{b} , but the second one is difficult to handle since the relations needed for \tilde{b} are nonlinear. This can result in large intensity differences even for small deviations of \tilde{b} from the ideal bit-value. The third point is a systematic problem since the preceding derivation assumed one wavelength to be mapped into one pixel only, but there will be small overlaps even for diffraction limited foci. In turn, these overlaps are controlled by the neighboring pixels, instead of the pixel that is responsible for this spectral component according to the wavelength to pixel-number mapping.

In summary, all three contributions could be minimized, but not excluded. Therefore a different approach is chosen. A feedback loop, i.e. an iterative algorithm, compares the imperfectly simulated spectrum to the desired reference spectrum. This reveals an intensity mismatch ΔI . For minimizing this mismatch, the algorithm computes the theoretical intensity difference for all wavelengths when decrementing \tilde{b} . This difference is compared to ΔI and \tilde{b} is adapted accordingly. However, the iterative algorithm proves to be more robust when the changes in the bit-values are subject to an upper limit. For example, the algorithm can start with a maximum difference of 300 (the possible values range from 0 to 4095) and reduce this limit in the subsequent iterations, e.g. 200 in the second one, 100 in the third one, 50 in the fourth and so forth. This has the advantage that the measured intensity does not break away from the desired value too much in case of an overcompensation by the algorithm and it can safely recover the initial value. The changes are subject to two further limits, to wit the maximum possible bit-value of 4095 and the value of darkbits at this wavelength. The following example clarifies this.

Consider a calculated bit-value of 3100 at some wavelength, an ideal (yet unknown) bit-value of 3025, a darkbit-value of 2900 and let the measured intensity be a little too high (say 10%). Since the phase change per bit-value difference is larger for smaller bit-values (cp. Fig. 17), the algorithm will overestimate the

needed change. To fill it with numbers, consider a calculated change of 600. This change is too large and reduced to the upper limit of 300 in a first step. The second limitation is the darkbit-value of 2900 the bit-value must not undershoot. This yields a corrected bit-value of 2900. The next iteration reveals a too low intensity (essentially zero). Since the intensity difference per bit-value difference around the darkbit-value is again low, the calculated correction will again exceed the upper limit of 200 for this iteration, resulting in a new bit-value of 3100. This is precisely the initial value, but at least the limitations circumvented something worse. The next iteration will yield a value of 3000 or higher, which is much closer to the optimum! The convergence to the optimum bit-value is rather slow in this (made-up) example, but the algorithm had at least the chance to converge faster. Generally, i.e. for most wavelengths, it takes this chance.

6.3 Experimental simulation of various spectra

6.3.1 Experimental procedures

All spectra^f are measured using a $f = 150$ mm monochromator (Acton SP2155) with two gratings ($600 \ell/\text{mm}$) at Blaze wavelengths of 500 and 1000 nm, respectively, resulting in a resolution of 1 nm at a slit width of $100 \mu\text{m}$. This resolution exceeds the required one for the IR part, but is marginal for the VIS range since the SLM resolution is 0.5 nm at the blue end of the spectrum.

The light is detected by a Si/PbS two-color-detector (Hamamatsu K3413-01). Edge filters are not required in the monochromator since second order diffraction can be blocked using the SLM. Furthermore, the PbS photoconductive detector (in the two-color-detector) is insensitive to visible light since it has been absorbed by the Si-photodiode being on top of the PbS photoconductive detector. One scan takes about 15 minutes to reach the signal to noise ratio in the following examples.

^fExcept the one in Fig. 9.

The IV-characteristics are measured using the circuit shown in Fig. 18. The voltage output is provided by a National Instruments USB 6009 AD/DA converter, while the current is measured using a current-to-voltage-converter⁵⁰ comprising an operational amplifier (Burr-Brown OPA129U), a resistor and a capacitor.

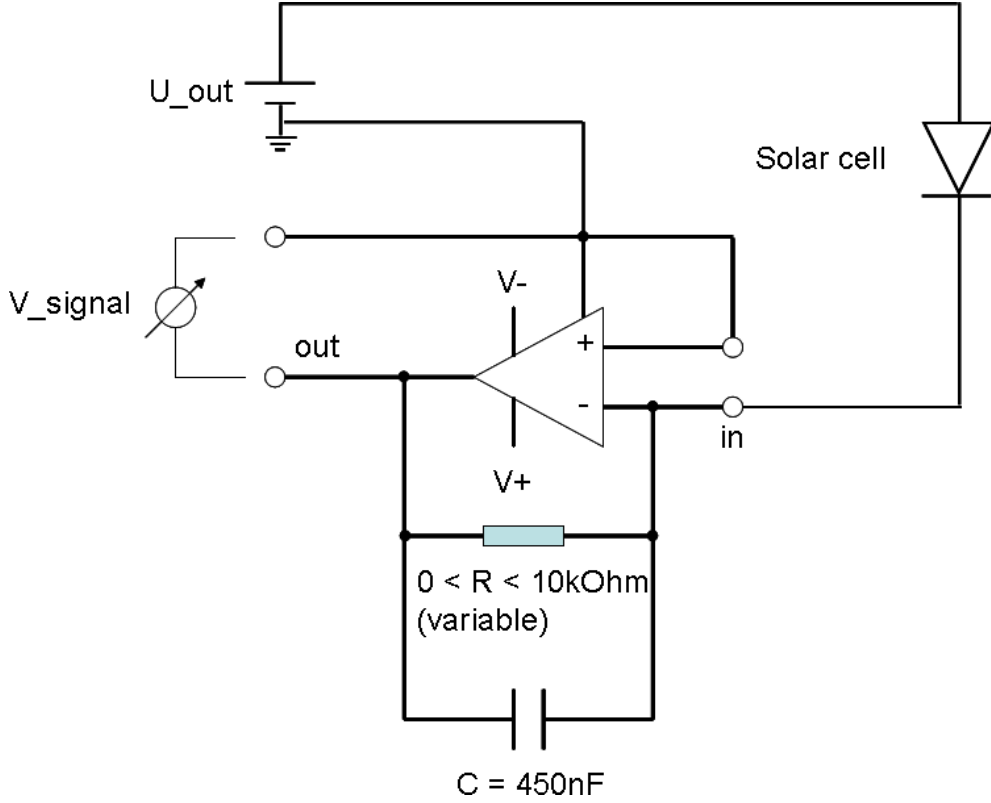


Figure 18: Electronic circuit for measuring the IV-characteristics of solar cells comprising a voltage source (U_{out}), a solar cell and a variable gain current-to-voltage-converter. The operational amplifier (Burr-Brown OPA129U) in the latter one is operated at $\pm 9\text{ V}$.

6.3.2 Flat spectrum

A first test of this procedure is the generation of a flat wavelength spectrum. The amplitude of the resulting spectrum is governed by the requirement that the ratio of I_T and I_{WLS} cannot exceed unity at any wavelength, i.e. the desired spectrum has to "fit" under I_{WLS} .

The choice to simulate a flat spectrum first provides the advantage of an excellent visibility of existing deviations. By this, one can get a quick impression of the quality of the simulated spectrum in the different spectral regions.

Fig. 19 (bottom) shows the simulated flat spectrum as the red curve, while the desired reference spectrum is shown as the black dotted line. The simulated spectrum exhibits a constant energy current density per wavelength of $j = 0.22 \text{ Wm}^{-2}\text{nm}^{-1}$ over the range from 480 to 1630 nm. Considering the illuminated area^g $A = \pi(4 \text{ mm})^2 \approx 50 \text{ mm}^2$ yields a spectral power density of $j_s = 0.22 \text{ Wm}^{-2}\text{nm}^{-1} \cdot 50 \text{ mm}^2 = 11 \mu\text{W}/\text{nm}$. The spectrally integrated power is then $P = 11 \mu\text{W}/\text{nm} (1630 \text{ nm} - 480 \text{ nm}) = 12.7 \text{ mW}$. Desired and measured spectrum show a very good match over the entire spectral range, except for the pump region around 1060 nm, where it is generally more difficult to get a good congruence. The deviation is quite large here, but not exceeding 20%, as confirmed by Fig. 19 (top). Even the sharp edges don't constitute a problem.

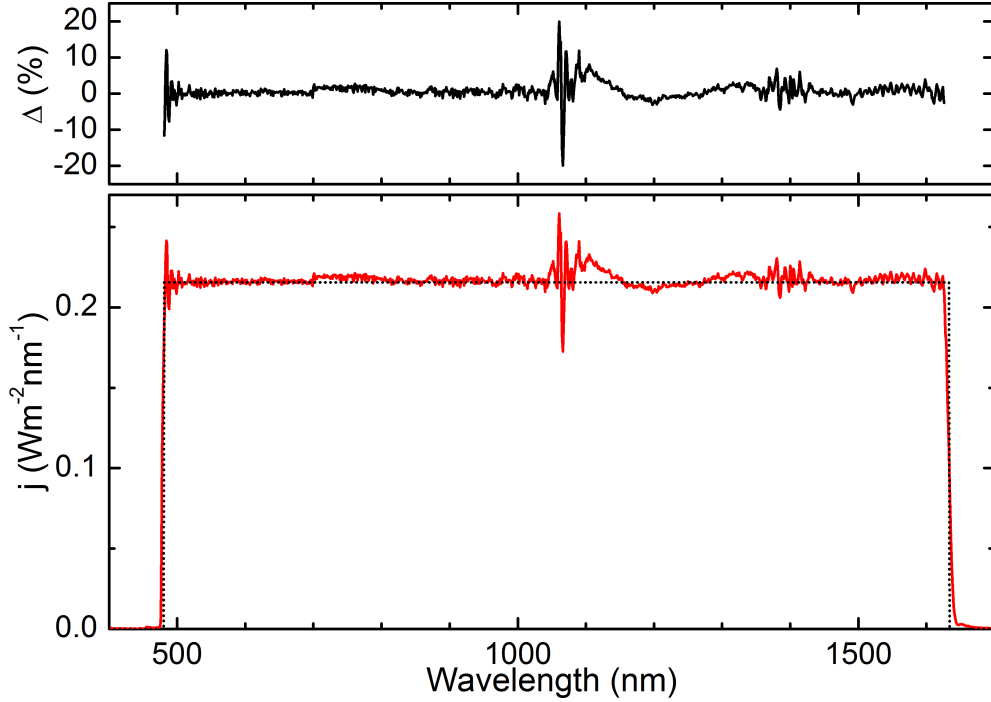


Figure 19: (bottom) Simulation of a spectrally flat optical spectrum extending from 480 nm to 1630 nm with a spectrally constant energy current density of $j = 0.22 \text{ Wm}^{-2}\text{nm}^{-1}$. Red solid line: Experimentally generated spectrum $j_{ex}(\lambda)$ using the optical synthesizer described in Fig. 1. Black dotted line: Desired reference spectrum $j_r(\lambda)$. (top) Relative deviation $\Delta(\lambda) = [j_{ex}(\lambda) - j_r(\lambda)] / j_r(\lambda)$ between experimentally generated and desired spectrum.

^gThe beam diameter is $\approx 8 \text{ mm}$.

6.3.3 Reference spectra AM0 and AM1.5G

Next, two internationally established reference spectra for testing solar cells, to wit, AM0⁵¹ and AM1.5G⁵², are simulated. The setup cannot cover the entire range, over which these spectra are defined, but at least a part of it. Both simulated spectra are shown as the red curves in Fig. 20, where the left one is the AM0 spectrum and the right one AM1.5G. Just like in the example for the flat spectrum, the convention of black dotted lines for the desired reference spectrum and red solid lines for the experimentally simulated spectra is adopted. The deviation is given in the respective top figures. In contrast to the previous example, the absolute instead of the relative deviation is shown since the spectrum is close to zero around 1400 nm. In turn, this results in extremely large relative deviations that are no longer representative for the quality of the simulated spectrum.

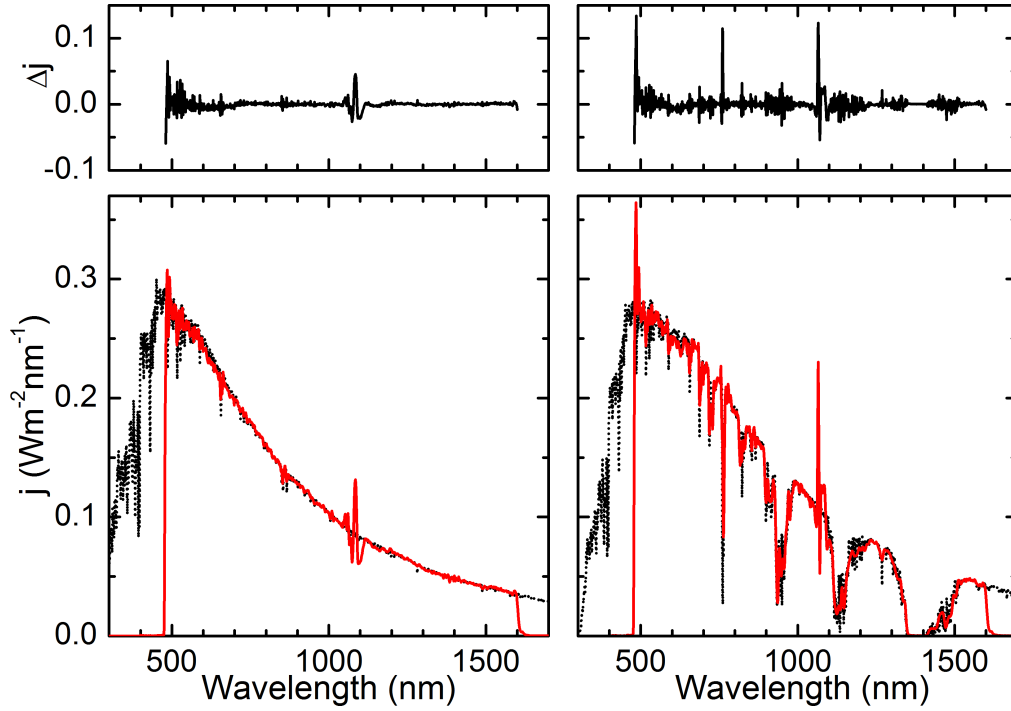


Figure 20: Red solid lines: Experimentally simulated AM0 (left) and AM1.5G (right) solar spectra generated using the optical synthesizer described in Fig. 1. Black dotted lines: Reference AM0⁵¹ and AM1.5G⁵² spectra, normalized to the energy current density of the experimentally measured spectra. (top) Difference $\Delta j(\lambda) = j_{ex}(\lambda) - j_r(\lambda)$ between experimental and normalized reference spectra for AM0 (left) and AM1.5G (right).

The spectrally integrated power is $P = 6.7 \text{ mW}$ for both spectra, while intuition demands a lower value for the AM1.5G spectrum due to the absorption losses in the atmosphere of the earth responsible for the minima. However, this intuitive picture lacks one important feature: Rayleigh scattering is responsible for a reduction of the amplitude at the blue end of the (AM1.5G) spectrum. After all, this part limits the amplitude of the simulated solar spectra since they have their maximum here, where I_{WLS} is quite low. In turn, solar spectra with a reduced amplitude in the blue regime can be simulated at a higher power. By coincidence, this exactly compensates for the absorption losses in the AM1.5G spectrum.

Generally, the fit is good for both spectra, but the AM1.5G spectrum shows two narrow peaks the algorithm could not suppress this time. Such peaks are likely to occur if either the reference or I_{WLS} are strongly changing with wavelength *and* the mapping of pixel-numbers to wavelengths is slightly wrong. The first condition is clearly satisfied at the two peaks: The reference spectrum jumps from zero to its global maximum at 480 nm and I_{WLS} is not smooth at 1060 nm (cp. Fig. 14). This implies that the wavelength to pixel-number mapping was indeed slightly inaccurate, although it cannot be checked at this stage since the mapping had to be recalculated for several reasons in between the experiments.

6.3.4 Summer and winter spectrum measured outdoors

Finally, two spectra that have been measured outdoors should be simulated. Besides pronouncing the versatility of the setup it gives an explicit example of how the solar spectrum changes in time. For this purpose, two spectra are chosen that have been measured in Stuttgart in summer (July) and winter (February), respectively⁵³. The comparison following the same scheme as used in the previous examples is given in Fig. 21, where the left one is the summer spectrum. The spectrally integrated power of the winter spectrum is $P = 7.9 \text{ mW}$ and higher than for the summer spectrum ($P = 7.2 \text{ mW}$) for the same reason the power of the AM1.5G spectrum is not lower than that of the AM0 spectrum.

This time, the intensity match of desired and reference spectra is even better than in the previous examples. For this reason, the absolute difference Δj has to be multiplied by 1000 in the respective top figures. This time, the desired spectra are restricted to the modulation range, i.e. they do possess spectral components beyond the two edges.

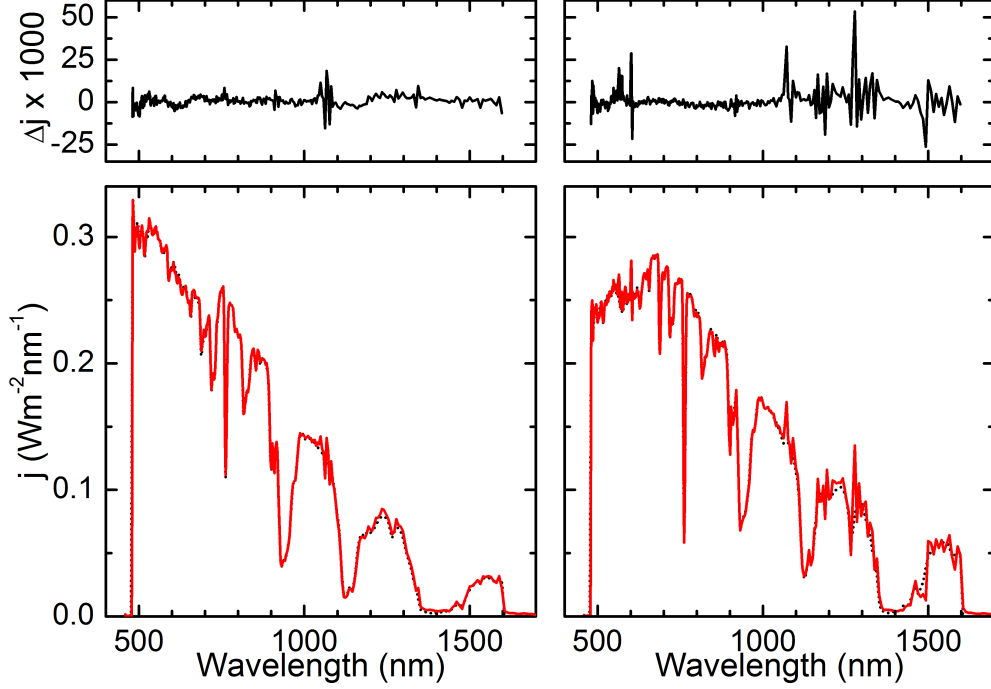


Figure 21: Red solid lines: Experimentally simulated summer (left) and winter (right) solar spectra generated using the optical synthesizer described in Fig. 8. Black dotted lines: Reference summer and winter spectra⁵³ measured in July and February, respectively. The spectra are normalized to the energy current density of the experimentally measured ones. (top) Difference $\Delta j(\lambda) = j_{ex}(\lambda) - j_r(\lambda)$ between experimental and normalized reference spectra for summer (left) and winter (right).

6.4 A first test with a triple-junction solar cell

Now, the setup is tested as a solar simulator. For this purpose, two spectra (AM1.5G and the winter spectrum in Fig. 21, bottom right) are simulated and a Ga_{0.50}In_{0.50}P/Ga_{0.99}In_{0.01}As/Ge triple-junction solar cell (bandgaps of 1.87/1.44/0.67 eV)⁵⁴ is illuminated with them. During this illumination the IV-characteristic is measured. This curve allows for the calculation of the maximum power the solar cell can deliver. Dividing this power by the incident light power yields the solar cell efficiency η .

The simulated spectra are pulsed and there exist measurements indicating an intensity dependent efficiency¹³. For this reason, the influence of the pulsed nature of the supercontinuum on the IV-characteristics has been carefully checked at different intensities showing no difference⁵⁵.

A solar cell with a diameter of 2 mm is placed in the middle of the 8 mm beam. For the calculation of the incident light power, the Gaussian beam profile has to be taken into account. Doing so yields an incident light power of $P_{in} = 3.98 \text{ mW}$ ($\hat{=}$ 1.27 suns) for the AM1.5G and $P_{in} = 4.94 \text{ mW}$ ($\hat{=}$ 1.57 suns) for the winter spectrum. The measured IV-characteristics are shown in Fig. 22.

The maximum power the solar cell can provide is $P = 1.28 \text{ mW}$ when illuminated by the winter spectrum (green) and thus higher than for the AM1.5G spectrum ($P = 1.11 \text{ mW}$, blue curve). Despite this higher power the efficiency is worse ($\eta \approx 26\%$) than for the AM1.5G spectrum ($\eta \approx 28\%$) due to the significantly higher incident light power.

The blue IV-characteristic features a current-level change of $60 \mu\text{A}$ at $\approx 0.6 \text{ V}$ in the otherwise approximately flat part of the (exponential) IV-characteristic. This change is clearly above the noise level of $\approx 10 \mu\text{A}$ and could be characteristic for current-limited multi-junction solar cells, but no systematic analysis has been carried out so far.

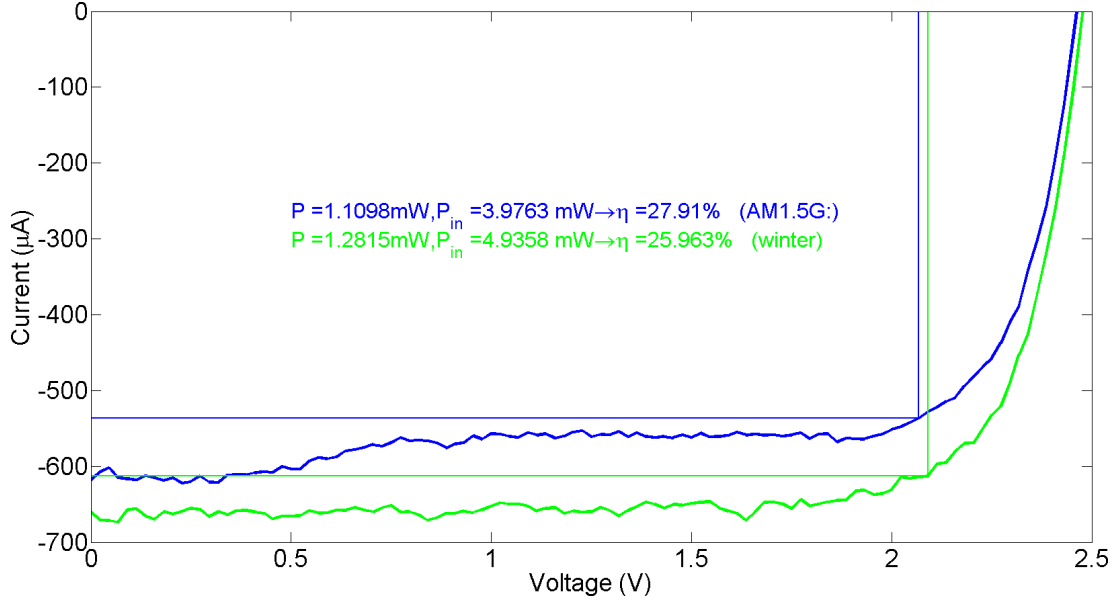


Figure 22: IV-characteristics of a Ga_{0.50}In_{0.50}P/Ga_{0.99}In_{0.01}As/Ge triple-junction solar cell (diameter 2 mm) with bandgaps of 1.87/1.44/0.67 eV under the winter spectrum in Fig. 21 (green) and under the AM1.5G spectrum in Fig. 20 (blue). Both curves have been averaged 300 times, but a noise level of $\approx 10 \mu\text{A}$ remains. The solar cell powers P are determined by maximizing the area of the respective rectangles. The incident light powers P_{in} are calculated by integrating over the measured spectrum and taking into account the Gaussian beam profile at a $1/e^2$ diameter of 7 mm. The efficiency η is then defined as P/P_{in} .

The noise level present in the IV-characteristics could not be minimized further despite the curve has been averaged 300 times. This noise is not due to the electronic measuring circuit, which is proven by measuring the dark IV-characteristic, as shown in Fig. 23. This curve shows a significantly reduced noise level ($\approx 0.2 \mu\text{A}$) and implies that the noise is due to the WLS.

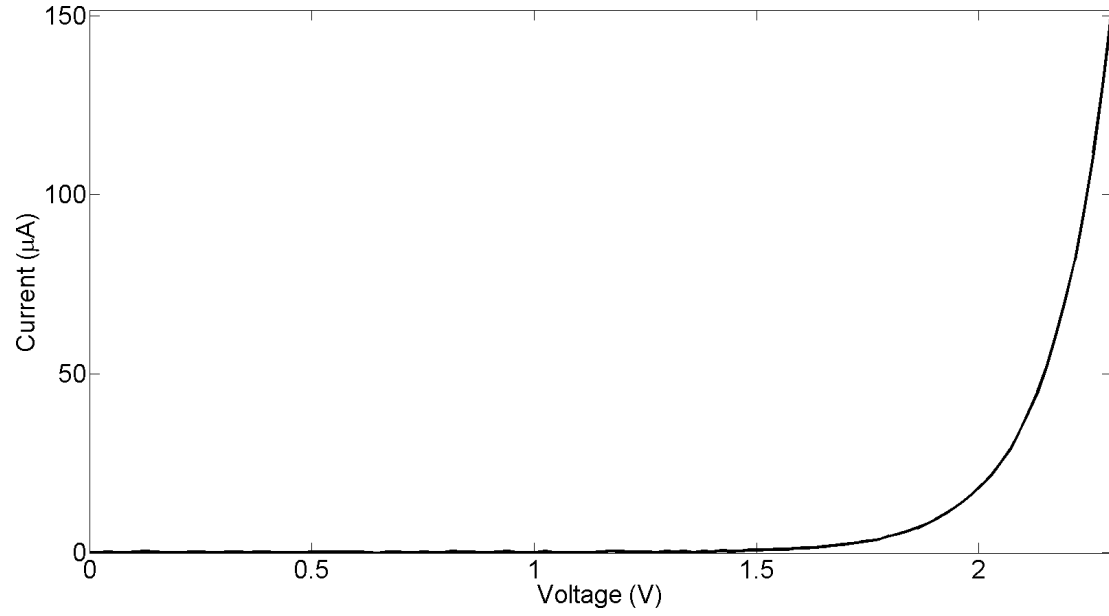


Figure 23: IV-characteristics of the same solar cell as in Fig. 22, but this time under no illumination. The noise level is at $\approx 0.2 \mu\text{A}$ showing that the significantly higher noise level in the IV-characteristics under illumination is not due to the electronic circuit, but due to the light source (WLS).

7 Conclusions and Outlook

Limitations and disadvantages

First of all, the limitations of this solar simulator are summarized. The first and most restrictive one is the spectral range. The WLS is not providing a sufficient amount of blue light beyond 480 nm. A replacement has to be found since this spectral part is essential for testing solar cells. One way would be placing a crystal that generates second harmonic light (i.e. light with half the incoming wavelength) in front of the synthesizer. Unfortunately, this cannot broaden the modulation range up to the 300 nm necessary for covering the entire solar spectrum at the short wavelength end since the SLM does not transmit UV light. A second option is an additional illumination of the solar cell with a blue diode. This will result in a much worse congruence of desired and reference spectrum compared to the current modulation range, but it's at least much better than a vanishing intensity. The WLS emits light in the IR spectral range (up to $2.3\text{ }\mu\text{m}$), but that light is absorbed by the SLM. Fortunately, this part is irrelevant for testing solar cells since most photons with wavelengths greater than 1600 nm are transmitted through high efficiency triple-junction solar cells anyway⁴⁻⁶.

Another limitation is the WLS spectrum as an upper limit to the energy current density of all spectra that can be simulated. This does not limit the possible spectral distributions, but the amplitude of the simulated spectra and, in turn, the solar cell area that can be illuminated with a desired spectrum and intensity. The setup presented in this thesis can simulate terrestrial solar spectra at a power of $\approx 7\text{ mW}$.

The third limitation is the spectral resolution of 0.5 nm in the VIS range and 8 nm at the IR end of the spectrum. This is no fundamental limit of the presented technique, but rather a question of the chosen prisms and mirrors in combination with the SLM (pixel pitch and number of pixels). This choice is governed by the desired spectral range, i.e. a spectrum of narrower bandwidth could be simulated at a higher precision.

The next limitation is the accuracy at which the intensity can be set. On the one hand this is determined by the resolution (2.44 mV) at which voltages can be applied to the individual SLM pixels. On the other hand its determined by the absolute bit-value since the DMC is no linear function. This causes different intensity increments per bit-value increment depending on the absolute bit value. Generally, the sensitivity is high, i.e. better than $1 \text{ mWm}^{-2}\text{nm}^{-1}$, at large bit-values (> 3000) and better than $5 \text{ mWm}^{-2}\text{nm}^{-1}$ for lower bit-values. The sensitivity is better in the VIS range than in the IR for solar spectra since lower bit-values are equivalent to a higher suppression of the WLS spectrum in that wavelength interval.

The remaining disadvantages are entirely due to the WLS. One is the inhomogeneous (Gaussian) intensity profile that allows only for very small solar cells to be illuminated approximately homogeneously. This poses yet another problem. Limiting the testing area changes the spectrum since it's changing with the distance from the center of the beam. This change is due to longer wavelengths being diffracted more by the small fiber of the white light fiber source than shorter wavelengths, which causes richer red spectra at larger radii. This disadvantage can be circumvented by focusing the light onto the solar cell which then entirely sacrifices homogeneity of illumination. The last disadvantage is the temporal instability of the WLS. First of all, this demands for a recalculation of the needed bit-values every time a spectrum should be simulated and limits the available measurement time until this spectrum changes ($\approx 30 \text{ min}$). Another problem due to this temporal instability is the noise in the IV-characteristics that needs to be reduced further.

Advantages

Despite all the limitations and disadvantages mentioned above, the presented setup is able to generate essentially arbitrary broadband optical spectra. Such a device has not yet been available. Commercially available solar simulators are capable of generating solar spectra over the entire range, but at a reduced quality^{14,18–20}.

Besides the (limited) capability for conventional testing schemes of solar cells, the effect of natural spatiotemporal variations in the solar spectrum can be simulated. This allows for the study its influence on the efficiency of photovoltaic systems. A further option is the ability to check which subcell is current limiting by just decreasing the intensity of some spectral part designated for a specific subcell. An entirely new possibility shows up with the ability to focus the simulated spectra onto very small spotsizes ($\approx 200 \mu\text{m}$) allowing for spatially resolved testing of solar cells.

Prospects for the future

The previously mentioned plans for covering the blue and UV part of the solar spectrum could allow for solar cells to be reliably tested under arbitrary spectra. Additionally, an interesting effect can be studied. This is seen in Fig. 22 (blue curve) as the deviation from the exponential IV-characteristic of a single pn-junction. It could be due to a current limitation of one of the subcells and is worth a systematic investigation.

References

- [1] W. Shockley and H.J. Queisser. Detailed balance limit of efficiency of p-n junction solar cells. *J. Appl. Phys.*, **32**:510–519, 1961.
- [2] G. Peharz, G. Siefer, and A.W. Bett. A simple method for quantifying spectral impacts on multi-junction solar cells. *Sol. En.*, **83**:1588–1598, 2009.
- [3] M.A. Green, K. Emery, Y. Hishikawa, and W. Warta. Solar cell efficiency tables (version 36). *Prog. Photov.*, **18**:346–352, 2010.
- [4] R. R. King, D. C. Law, K. M. Edmondson, C. M. Fetzer, G. S. Kinsey, H. Yoon, R. A. Sherif, and N. H. Karam. 40% efficient metamorphic GaInP/GaInAs/Ge multijunction solar cells. *Appl. Phys. Lett.*, **90**:183516, 2007.
- [5] J. F. Geisz, D. J. Friedman, J. S. Ward, A. Duda, W. J. Olavarria, T. E. Moriarty, J. T. Kiehl, M. J. Romero, A. G. Norman, and K. M. Jones. 40.8% efficient inverted triple-junction solar cell with two independently metamorphic junctions. *Appl. Phys. Lett.*, **93**:123505, 2008.
- [6] W. Guter, J. Schöne, S.P. Philipps, M. Steiner, G. Siefer, A. Wekkeli, E. Welser, E. Oliva, A.W. Bett, and F. Dimroth. Current-matched triple-junction solar cell reaching 41.1% conversion efficiency under concentrated sunlight. *Appl. Phys. Lett.*, **94**:223504, 2009.
- [7] B. E. Sağol, U. Seidel, N. N. Szabó, K. Schwarzburg, and T. Hannappel. Basic concepts and interfacial aspects of high-efficiency III-V multijunction solar cells. *Chimia*, **61**:775–779, 2007.
- [8] G. Létay, C. Baur, and A. W. Bett. Theoretical investigations of III-V multijunction concentrator cells under realistic spectral conditions. In *19th Europ. Photov. Sol. En. Conf.*, pages 187–190, 2004.

- [9] R. R. King, C. M. Fetzer, D. C. Law, K. M. Edmondson, H. Yoon, G. S. Kinsey, D. D. Krut, J. H. Ermer, P. Hebert, B. T. Cavicchi, and N. H. Karam. Advanced III-V multijunction cells for space. In *4th World Conference on Photov. En. Conv.*, pages 1757–1762, 2006.
- [10] W. G. J. H. M. van Sark. Simulating performance of solar cells with spectral downshifting layers. *Thin Solid Films*, **516**:6808–6812, 2008.
- [11] H. Mülleijans, A. Ioannides, R. Kenny, W. Zaaïman, H.A. Ossenbrink, and E.D. Dunlop. Spectral mismatch in calibration of photovoltaic reference devices by global sunlight method. *Meas. Sci. Technol.*, **16**:1250–1254, 2005.
- [12] G. Peharz, G. Siefer, K. Araki, and A.W. Bett. Spectrometric outdoor characterization of cpv modules using isotype monitor cells. *33rd IEEE Specialist Conference*, 2008. doi: 10.1109/PVSC.2008.4922735.
- [13] M. Meusel, C. Baur, G. Siefer, F. Dimroth, A.W. Bett, and W. Warta. Characterization of monolithic III-V multi junction solar cells – challenges and application. *Sol. En. Mat. and Sol. Cells*, **90**:3268–3275, 2006.
- [14] G. Siefer, C. Baur, M. Meusel, F. Dimroth, A.W. Bett, and W. Warta. Influence of the simulator spectrum on the calibration of multi-junction solar cells under concentration. *29th IEEE Specialist Conference*, pages 836–839, 2002.
- [15] P. Faine, S.R. Kurtz, C. Riordan, and J.M. Olson. The influence of spectral solar irradiance variations on the performance of selected single-junction and multijunction solar cells. *Solar Cells*, **31**:259–278, 1991.
- [16] R.W. Mueller, K.F. Dagestad, P. Ineichen, M. Schroedter-Homscheidt, S. Cros, D. Dumortier, R. Kuhlemann, J.A. Olseth, G. Piernavieja, C. Reise, L. Wald, and D. Heinemann. *Remote Sensing of Environment*, volume **91**, Article Rethinking satellite-based solar irradiance modelling – The SOLIS clear-sky module, pages 160–174. Elsevier Science Inc., 2004.

- [17] G. Seckmeyer and H.-D. Payer. A new sunlight simulator for ecological research on plants. *J. Photochem. Photobiol., B: Biol.*, **21**:175–181, 1993.
- [18] M. Meusel, R. Adelhelm, F. Dimroth, A. W. Bett, and W. Warta. Spectral mismatch correction and spectrometric characterization of monolithic III-V multi-junction solar cells. *Prog. Photov.*, **10**:243–255, 2002.
- [19] C. Domínguez, I. Antón, and G. Sala. Solar simulator for concentrator photovoltaic systems. *Optics Express*, **16**:14894–14901, 2008.
- [20] M. Bliss, T. R. Betts, and R. Gottschalg. An LED-based photovoltaic measurement system with variable spectrum and flash speed. *Sol. En. Mat. and Sol. Cells*, **93**:825–830, 2009.
- [21] Fianium. *Supercontinuum SC450*, January 14th, 2010. URL <http://www.fianium.com/products/optical.htm>.
- [22] I. Riedel. Solarzelle. Anleitung Blockpraktikum FPR-B, C.v.O. Universität Oldenburg, 2008.
- [23] C.H. Henry. Limiting efficiencies of ideal single and multiple energy gap terrestrial solar cells. *J. Appl. Phys.*, **51**:4494–4500, 1980.
- [24] J. Britt and C. Ferekides. Thin-film CdWCdTe solar cell with 15.8% efficiency. *Appl. Phys. Lett.*, **62**:2851–2852, 1993.
- [25] T. Zdanowicz, T. Rodziewicz, and M. Zabkowska-Waclawek. Theoretical analysis of the optimum energy band gap of semiconductors for fabrication of solar cells for applications in higher latitudes locations. *Sol. En. Mat. and Sol. Cells*, **87**:757–769, 2005.
- [26] M. Hermle, G. Létay, S. P. Philipps, and A. W. Bett. Numerical simulation of tunnel diodes for multi-junction solar cells. *Prog. Photovolt.*, **16**:409–418, 2008.

- [27] A. Luque and S. Hegedus, editors. *Handbook of photovoltaic science and engineering*. Wiley-VCH, 2003.
- [28] G. Conibeer. Third-generation photovoltaics. *Materials Today*, **10**:42–50, 2007.
- [29] H. Hovel. *Solar Cells*. Academic Press, New York, **11th** edition, 1975.
- [30] I. Riedel. Grundlagen der Photovoltaik. Lecture Notes, C.v.O. Universität Oldenburg, 2009.
- [31] N.W. Ashcroft and N.D. Mermin. *Festkörperphysik*. Oldenbourg, 2007.
- [32] C. Kittel. *Einführung in die Festkörperphysik*. Oldenbourg, 2005.
- [33] P. Würfel. *Physics of Solar Cells*. Wiley-VCH, 2009.
- [34] T. Muneer. *Solar radiation and daylight modes*. Elsevier, 2004.
- [35] L. Rayleigh. On the transmission of light through an atmosphere containing small particles in suspension, and on the origin of the blue of the sky. *Philos. Mag.*, **47**:375–384, 1899.
- [36] A.G. Rojo and P.R. Berman. Rayleigh scattering revisited: From gases to crystals. *Am. J. Phys.*, **78**:94–101, 2010.
- [37] T. Behrendt, A. Hammer, E. Lorenz, and D. Heinemann. Spektrale Solarstrahlung aus Satellitendaten zur Bewertung des Leistungsverhaltens von Dünnschicht-Solarzellen. Staffelstein, Germany, March 2009. 24. Symposium Photovoltaische Solarenergie.
- [38] T. R. Betts. *Investigation of Photovoltaic Device Operation under Varying Spectral Conditions*. PhD thesis, Loughborough University, 2004.
- [39] A.M. Weiner, J.P. Heritage, and E.M. Kirschner. High-resolution femtosecond pulse shaping. *J. Opt. Soc. Am. B*, **5**:1563–1572, 1988.

- [40] A.M. Weiner. Femtosecond pulse shaping using spatial light modulators. *Rev. Sci. Instr.*, **71**:1929–1960, 2000.
- [41] G. Stobrawa. *Aufbau und Anwendungen eines hochauflösenden Impulsformers zur Kontrolle ultrakurzer Laserimpulse*. PhD thesis, Friedrich-Schiller-Universität Jena, 2003.
- [42] T. Binhammer. *Erzeugung und Anwendung geformter Laserpulse mit oktaubreitem Spektrum*. PhD thesis, Ruprecht-Karls-Universität Heidelberg, 2006.
- [43] E. Hecht and A. Schleitner. *Optik*. Oldenbourg, fourth edition, 2009.
- [44] W. Schmidt. Phasenkontrolle von wenig-Zyklen Lichtimpulsen. Master’s thesis, 2009.
- [45] Cambridge Research and Instrumentation Inc. *Spatial Light Modulator (SLM) System User’s Manual*, 1.3 edition, June 2004.
- [46] D. J. Griffiths. *Introduction to Electrodynamics*. Prentice Hall International, third edition, 2003.
- [47] Thorlabs, 16.11.2010. URL <http://www.thorlabs.com/catalogpages/v20/764.pdf>.
- [48] Edmund Optics, 26.10.2010. URL <http://www.edmundoptics.com/images/articles/curve.gif>.
- [49] Schott. Optisches Glas. Data sheet, September 9th, 2009.
- [50] P. Horowitz and W. Hill. *The art of electronics*. Cambridge University Press, 1980.
- [51] American Society for Testing and Materials. ASTM G-173 AM0.
- [52] American Society for Testing and Materials. ASTM G-173 AM1.5 global. (IEC 60904-3, Ed. 2), 2008.

- [53] Private communication with Annette Hammer, University of Oldenburg.
- [54] Private communication with Gerhard Peharz, Dept. Materials – Solar Cells and Technology, Fraunhofer-Institut für Solare Energie Systeme.
- [55] E. Sommer and T. Bienert. Variation des Strahlungsspektrums für neue Solarenergietechnologien. Bachelor's Thesis, C.v.O. Universität Oldenburg, November 2009.

A Appendix to Eq. 17

To be solved:

$$2 \langle \cos(kz - \omega t + \varphi) \cos(kz - \omega t) \rangle_t$$

Using the trigonometric identity $\cos(\alpha + \beta) = \cos(\alpha) \cos(\beta) - \sin(\alpha) \sin(\beta)$ the relation above can be transformed according to

$$2 \langle \cos(kz - \omega t + \varphi) \cos(kz - \omega t) \rangle_t$$

$$= 2 \langle [\cos(kz - \omega t) \cos(\varphi) - \sin(kz - \omega t) \sin(\varphi)] \cos(kz - \omega t) \rangle_t$$

$$= 2 \langle \cos^2(kz - \omega t) \cos(\varphi) - \sin(kz - \omega t) \cos(kz - \omega t) \sin(\varphi) \rangle_t$$

$$= 2 \underbrace{\langle \cos^2(kz - \omega t) \rangle_t}_{=\frac{1}{2}} \cos(\varphi) - 2 \underbrace{\langle \sin(kz - \omega t) \cos(kz - \omega t) \rangle_t}_{=0} \sin(\varphi)$$

$$= \cos(\varphi)$$

B List of components

- Light source: Fianium SC-450-4
- $3 \times 3''$ parabolic on-axis mirror, $f = 444.5$ mm, protected Al coating, Edmund Optics, NT 32-064-522
- $2 \times$ Glan Laser polarizing beam splitter, GL10
- $2 \times$ flat mirror, $60 \text{ mm} \times 85 \text{ mm}$ silver coating, Linos Photonics, G 340662000
- $2 \times$ SF 4 prism, $60^\circ \pm 5''$, edges $(50 \pm 0.2) \text{ mm}$, height $(50 \pm 0.1) \text{ mm}$, Hellma Optik
- LCD-SLM: 640 pixels, display $64 \text{ mm} \times 5 \text{ mm}$, pixel size $100 \mu\text{m} \times 5 \text{ mm}$, 12 bit resolution, Cambridge Research and Instrumentation (CRI), SLM-640-D-NM
- 90° off-axis parabolic mirror, diameter 25.4 mm, effective focal length 152.4 mm, protected Al coating, Edmund Optics, #63-184
- Monochromator: Acton SP-2155, $f = 150 \text{ mm}$, gratings
 - $32 \text{ mm} \times 32 \text{ mm}$, $600 \ell/\text{mm}$, 500 nm Blaze, Roper Scientific, 150-060-500
 - $32 \text{ mm} \times 32 \text{ mm}$, $600 \ell/\text{mm}$, $1 \mu\text{m}$ Blaze, Roper Scientific, 150-060-1
- Photodetector: Hamamatsu Photonics
 - Si/PbS two-color-detector, K3413-01
 - Heatsink, A3179-03
 - Temperature Controller, C1103-04
 - Si photosensor amplifier, C9329
 - PbS preamplifier, C3757-02

- Optical Chopper: Thorlabs, MC2000, 10-slot blade
- Lock-In amplifier: Femto, LIA-MVD-200-H
- AD/DA Converter: National Instruments, USB 6009, 14 bit
- Current to Voltage converter: Burr-Brown OPA129U

C Reflection efficiencies for used coatings

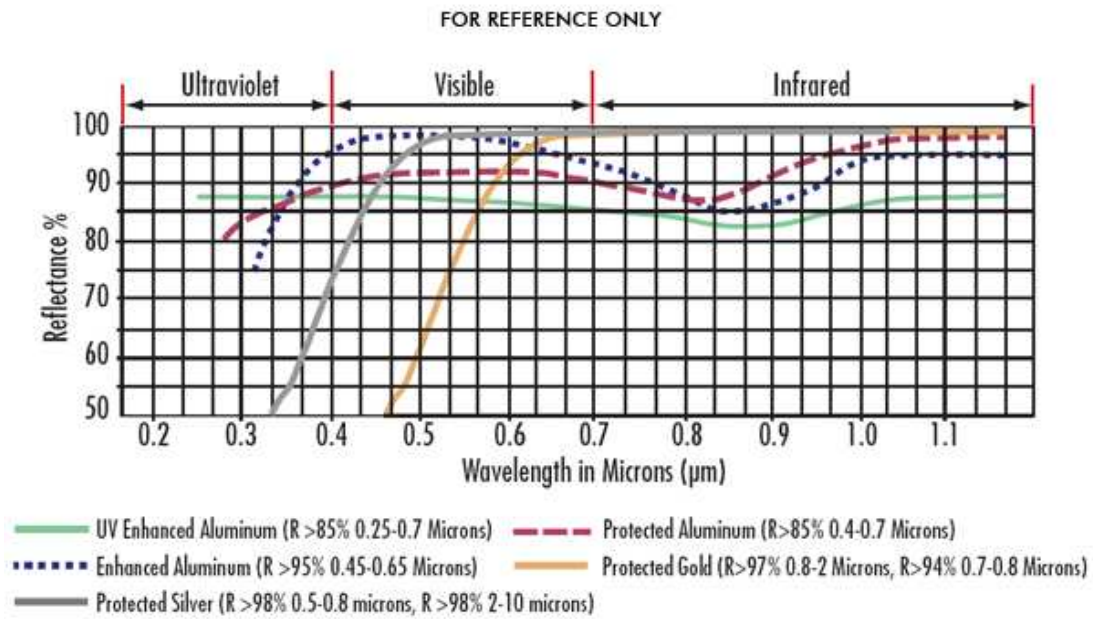


Figure 24: Reflection efficiencies for used coatings, from⁴⁸. We have in use protected Al (red dashed line) as well as protected Ag (grey solid line).

D Source code for MATLAB

D.1 Raytracing

```
clear all
close all
clc

% Functions needed:
% - schnittpunkt (calculates the intersection of the light ray with
the
%               parabolic mirror)
% - phi_r (calculates phi_r)
% - ray (calculates ray-vectors that can be plotted)

D = 100;    % mirror diameter
f = 444.5;  % focal length (mm)
a = 1/(4*f); %  $x = a*y^2$ 
w = 8;      % (visible) beam diameter
phi_i = -4.1; % incident angle (blue)
phi_i3 = phi_i + 8.2; % incident angle (red)
x_P = f;    % prism position
y_P = 0;    %

% light ray 1 (blue)
[x_SC,y_SC] = schnittpunkt(x_P,y_P,phi_i,a);
phi_rC = phi_r(phi_i,a,y_SC);
phi_rC1 = phi_rC;
[ray_iC1(1,:),ray_iC1(2,:),ray_rC1(1,:),ray_rC1(2,:)] =
rayL(phi_i,phi_rC,x_SC,y_SC,f,f);

% code explanation:
% ray_iC1: i for incoming (possible: i,r), C for Center ray
(C,Left,Right),
% 1 is ray number (1,2)
```

```

x_FL = x_P-w/2/sin(phi_i*pi/180);
[x_SL,y_SL] = schnittpunkt(x_FL,y_P,phi_i,a);
phi_rL = phi_r(phi_i,a,y_SL);
[ray_iL1(1,:),ray_iL1(2,:),ray_rL1(1,:),ray_rL1(2,:)] =
rayL(phi_i,phi_rL,x_SL,y_SL,f,f);

x_FR = x_P+w/2/sin(phi_i*pi/180);
[x_SR,y_SR] = schnittpunkt(x_FR,y_P,phi_i,a);
phi_rR = phi_r(phi_i,a,y_SR);
[ray_iR1(1,:),ray_iR1(2,:),ray_rR1(1,:),ray_rR1(2,:)] =
rayL(phi_i,phi_rR,x_SR,y_SR,f,f);

% light ray 2 was reserved for a green one in between

% light ray 3 (red)
[x_SC,y_SC] = schnittpunkt(x_P,y_P,phi_i3,a);
phi_rC = phi_r(phi_i3,a,y_SC);
phi_rC3 = phi_rC;
[ray_iC3(1,:),ray_iC3(2,:),ray_rC3(1,:),ray_rC3(2,:)] =
rayL(phi_i3,phi_rC,x_SC,y_SC,f,f);

x_FL = x_P-w/2/sin(phi_i3*pi/180);
[x_SL,y_SL] = schnittpunkt(x_FL,y_P,phi_i3,a);
phi_rL = phi_r(phi_i3,a,y_SL);
[ray_iL3(1,:),ray_iL3(2,:),ray_rL3(1,:),ray_rL3(2,:)] =
rayL(phi_i3,phi_rL,x_SL,y_SL,f,f);

x_FR = x_P+w/2/sin(phi_i3*pi/180);
[x_SR,y_SR] = schnittpunkt(x_FR,y_P,phi_i3,a);
phi_rR = phi_r(phi_i3,a,y_SR);
[ray_iR3(1,:),ray_iR3(2,:),ray_rR3(1,:),ray_rR3(2,:)] =
rayL(phi_i3,phi_rR,x_SR,y_SR,f,f);

```

```

%%%%%%%%%%%%%%%%%%%%%%%%%%%%%%%%%%%%%%%%%%%%%%%%%%%%%%%%%%
% plot-part
% *****
Sx = [1,0]; % select x-values
Sy = [0,1]; % select y-values
% *****
basis = 0 : 0.1 : a*(D/2)^2;

mirror_U = [basis;sqrt(basis/a)]; % upper half of mirror (Up)
mirror_D = [basis;-sqrt(basis/a)]; % lower half of mirror (Down)
% *****
% SLM (spatial light modulator)
x_c = f; % center
L = 39; % length of SLM
B = 325; % width of SLM
SLM = [x_c-L/2,x_c+L/2,x_c+L/2,x_c-L/2,x_c-L/2;-B/2,-
B/2,B/2,B/2,-B/2];
L = 1; % length of LCD
B = 64; % width of LCD
LCD = [x_c-L/2,x_c+L/2,x_c+L/2,x_c-L/2,x_c-L/2;-B/2,-
B/2,B/2,B/2,-B/2];
% *****

```

```

figure
% parabolic mirror
plot(Sx*mirror_U,Sy*mirror_U,'k',Sx*mirror_D,Sy*mirror_D,'k','
linewidth',3)
hold on
% LCD-SLM
% plot(Sx*SLM,Sy*SLM,'k')
plot(Sx*LCD,Sy*LCD,'k')
% prism
% plot(x_P,y_P,'ko')
% ray 1
plot(Sx*ray_iC1,Sy*ray_iC1,'b',Sx*ray_rC1,Sy*ray_rC1,'b','linewi
dth',2)
plot(Sx*ray_iL1,Sy*ray_iL1,'b',Sx*ray_rL1,Sy*ray_rL1,'b','linewi
dth',2)
plot(Sx*ray_iR1,Sy*ray_iR1,'b',Sx*ray_rR1,Sy*ray_rR1,'b','linewi
dth',2)
% ray 3
plot(Sx*ray_iC3,Sy*ray_iC3,'r',Sx*ray_rC3,Sy*ray_rC3,'r','linewi
dth',2)
plot(Sx*ray_iL3,Sy*ray_iL3,'r',Sx*ray_rL3,Sy*ray_rL3,'r','linewi
dth',2)
plot(Sx*ray_iR3,Sy*ray_iR3,'r',Sx*ray_rR3,Sy*ray_rR3,'r','linewi
dth',2)
text(f-13,40,'LCD','fontsize',28)
text(10,0,'PM','fontsize',28)
% general settings
set(gca,'fontsize',28)
xlabel('x (mm)')
ylabel('y (mm)')
axis equal
axis([-10 470 -50 50])
hold off

```



```

function [x_S,y_S] = schnittpunkt(x_P,y_P,phi_i,a)
% Parameters (x_P,y_P,phi_i,a)
% phi_i in degrees!

phi = phi_i*pi/180; % conversion of phi to radian

% y-intercept of incoming ray
b = (x_P + y_P/tan(phi))/a;

if phi_i==0
    y_S = y_P;
else
    help = 1/(2*a*tan(phi));
    if phi > 0
        y_S = -help + sqrt(help^2 + b);
    else
        y_S = -help - sqrt(help^2 + b);
    end
end

x_S = a*y_S^2;

function [x_i,y_i,x_r,y_r] = rayL(phi_i,phi_r,x_S,y_S,L_i,L_r)
% Parameters (phi_i,phi_r,x_S,y_S,L_i,L_r)

% incoming light ray
x_i = [x_S,x_S + L_i*cos(phi_i*pi/180)];
y_i = [y_S,y_S - L_i*sin(phi_i*pi/180)];

% reflected light ray
x_r = [x_S,x_S + L_r*cos(phi_r*pi/180)];
y_r = [y_S,y_S + L_r*sin(phi_r*pi/180)];

function phi_r = phi_r(phi_i,a,y_S)
% Parameters (phi_i,a,y_S)

phi_r = phi_i - 2*atan(2*a*y_S)*180/pi;

```

D.2 SLM-control

```
clear all
close all
clc

n = 6;
%[1 = transmission, 2 = dark, 3 = ohneVIS, 4 = drivecount, 5 =
drivecount-ohneVIS, 6 = drivecount_corr, 7 = drivecount_corr-
ohneVIS, 8 = individual]
F = 31; % frame number [0,31]
levels = 4095*ones(640,8);

darkbits = load('darkbits');
levels(:,2) = darkbits;

% individual = levels(:,8);
individual = darkbits;
pixel = 320;
% individual(pixel) = darkbits(pixel);
individual(pixel) = 4095;
%
% WLS reproducibility measurements
% 1)
% n = 3 % (without VIS)
levels(:,3) = levels(:,2);
levels(1:300,3) = 4095;
% 2)
% n = 1 % (transmission)
% 3)
% n = 2 % (dark)
```

```

% user defined drivecount
load('drivecount')
levels(:,4) = drivecount;
levels(:,5) = drivecount;
levels(300:end,5) = darkbits(300:end);
load('drivecount_corr')
levels(:,6) = drivecount_corr;
levels(:,7) = drivecount_corr;
levels(300:end,7) = darkbits(300:end);

% blau
% individual(580:end) = 4095;
% grün
% individual(450:480) = 4095;
% rot
% individual(280:300) = 4095;

%individual(294) = 4095;

levels(:,8) = individual;
stat = SlmInit('Com4','USB',640,'PHS+AMP');
if stat~=1
    msgbox('An error has occurred!','SlmInit','error')
    'Error code:'
    stat
end
stat = SlmSelectMask(1);
if stat~=1
    msgbox('An error has occurred!','SlmSelectMask','error')
    'Error code:'
    stat
end

```

```

stat = SlmDefineFrame(F,levels(:,1));
if stat~=1
    msgbox('An error has occurred!','SlmDefineFrame','error')
    'Error code:'
    stat
end

stat = SlmSelectFrame(F);
if stat~=1
    msgbox('An error has occurred!','SlmSelectFrame','error')
    'Error code:'
    stat
end

drive = SlmReadFrame(F);
if length(drive) == 1
    msgbox('An error has occurred!','SlmReadFrame','error')
    'Error code:'
    drive
end

% compare
if drive == levels(:,1)
    msgbox('Data transferred successfully!','Data transfer')
else
    msgbox('Data transfer not successful!','Data transfer','error')
end
stat = SlmSelectMask(0);
if stat~=1
    msgbox('An error has occurred!','SlmSelectMask','error')
    'Error code:'
    stat
end

```

```

stat = SlmDefineFrame(F,levels(:,n));
    if stat~=1
        msgbox('An error has occurred!','SlmDefineFrame','error')
        'Error code:'
        stat
    end
stat = SlmSelectFrame(F);
    if stat~=1
        msgbox('An error has occurred!','SlmSelectFrame','error')
        'Error code:'
        stat
    end
drive = SlmReadFrame(F);
    if length(drive) ==1
        msgbox('An error has occurred!','SlmReadFrame','error')
        'Error code:'
        drive
    end

% compare
if drive == levels(:,n)
    msgbox('Data transferred successfully!','Data transfer')
else
    msgbox('Data transfer not successful!','Data transfer','error')
end
stat = SlmGetError;
if stat ~= 0
    msgbox('An error has occurred!','Closing Sequence','error')
    stat
    SlmClearError
end
stat = SlmClose;

```


D.3 Prism deflection angle

```
% loading refractive index data (SCHOTT)
n = load('all.txt');
% loading the related wavelength basis
load('lambda.txt')
alpha = 60*pi/180; % prism angle
theta = atan(n(:,4)); % incident (Brewster) angle for 1060nm
u = ones(1,length(lambda));
% delta is the deviation angle matrix, materials along the rows,
% wavelengths along the columns
delta = theta*u + asin(sin(alpha)*sqrt(n.^2 - sin(theta).^2*u) -
sin(theta)*cos(alpha)*u) -
alpha*ones(length(theta),length(lambda));
delta = delta*180/pi; % conversion to degree
'difference-angle (DA) ='
DA = delta(:,end)-delta(:,1);
% from 480 to 2325nm
% first column of DA is a running index for the materials
DA = [(1:1:length(theta))',DA];

figure
plot(DA(:,1),DA(:,2),'k+', 'LineWidth',2, 'MarkerSize',40)
hold on
plot([1,length(theta)], [8.2,8.2], 'k', 'linewidth',3)
plot(DA(39,1),DA(39,2), 'or', 'linewidth',2, 'markersize',40)
text(34,8.4, 'N-LAF 36', 'fontsize',28)
plot(DA(55,1),DA(55,2), 'or', 'linewidth',2, 'markersize',40)
text(49,8, 'N-LASF 44', 'fontsize',28)
plot(DA(95,1),DA(95,2), 'or', 'linewidth',2, 'markersize',40)
text(92,8.4, 'SF 4', 'fontsize',28)
axis([0 105 7 9])
set(gca, 'fontsize',28)
set(gca, 'linewidth',2)
xlabel('Glass # (Schott)')
ylabel('Angle between 480nm and 2325nm (°)')
hold off
```

E Acknowledgements

I would like to give special thanks to all people having contributed to this work now.

First of all, I want to thank Prof. Dr. Christoph Lienau for the opportunity to work on this interesting project and his support as a first supervisor.

Special thanks go to my second supervisor Dr. Annette Hammer, too, for her active support.

Next, I want to thank Raimond Angermann for his continuous support as a technical assistant as well as Boris Groß for his help regarding the operational amplifier.

Furthermore, I want to thank Robert Pomraenke, Dr. Parinda Vasa, Dr. Martin Silies, Bernd Schwenker and Slawa Schmidt for many helpful discussions.

Thanks go to the entire UNO-group, too, for the pleasant working atmosphere, especially to my office mates Diyar Sadiq, Heiko Kollmann and Björn F. Piglosiewicz.

Last but not least, I want to thank my parents for their support.

Erklärung

Hiermit versichere ich, dass ich diese Arbeit selbständig verfasst und keine anderen als die angegebenen Quellen und Hilfsmittel benutzt habe. Außerdem versichere ich, dass ich die allgemeinen Prinzipien wissenschaftlicher Arbeit und Veröffentlichung, wie sie in den Leitlinien guter wissenschaftlicher Praxis der Carl von Ossietzky Universität Oldenburg festgelegt sind, befolgt habe.